https://doi.org/10.5194/egusphere-2026-523
Preprint. Discussion started: 6 February 2026

Coherent Modes of Northern Hemisphere Wind Extremes and Their Links to Global Large-Scale Drivers

Kai Bellinghausen[1], Birgit Hünicke[1], and Eduardo Zorita[1]

[1]Institute for Coastal System Analysis and Modelling, Helmholtz-Zentrum Hereon, Geesthacht (Germany)

Correspondence: Kai Bellinghausen (kai.bellinghausen@hereon.de)

Abstract. Analogously to the well-known seasonal atmospheric circulation patterns that capture coherent large-scale regions of synchronous variability (e.g. North Atlantic Oscillation) we aim in this study to identify spatially coherent modes of stormy seasons over the Northern Hemisphere (NH) land regions. Locally, stormy seasons are defined here as seasons with a high number of days having daily wind speed higher than the local climatological 95th-percentile derived from ERA5 reanalysis data. Applying a Principal Component Analysis (PCA) to seasonal October-through-March (ONDJFM) local storm indices reveals a leading mode of hemispheric variability characterised by a meridional dipole structure.

Regions north of 50° N (Europe–Asia) fluctuate coherently, in opposite phase to those farther south. Correlation analyses between the principal component time series and global spatial fields of Sea Surface Temperature (SST), Mean Sea Level Pressure (MSLP), and skin temperature (i.e. surface temperature at radiative equilibrium; SKT) identify teleconnections to the North Atlantic Oscillation (NAO) and Pacific SST anomalies, indicating that known climate modes modulate the large-scale spatial coherence of seasonal extreme wind frequency. These teleconnections to large-scale modes arise in the months preceding the target season ONDJFM, suggesting potential predictability at seasonal timescales.

To explore physical causality between SKT and storminess modes related to the atmospheric response to SKT-anomalies, we use the atmospheric emulator ACE2 driven at the surface by the relevant patterns of SKT identified in the SKT–storm correlation analysis. The ACE2 emulator is a recently released artificial-intelligence emulator trained with ERA5 reanalysis. The emulator experiments reproduce the observed storm variability pattern and yield a split jet-stream response with both poleward and equatorward branches. ACE2 simulations driven by the relevant patterns of SKT do tend to produce more stormy seasons in the regions identified by the mentioned PCA analysis. These results support a causal link between coherent large-scale patterns of seasonal storminess and large-scale surface temperature gradients.

Our findings bridge statistical climate variability with physical processes, offering a framework for understanding how continental storm risks respond to changes in global surface temperature. We note that this framework can also be applied to other extreme events.

Plain Language Summary: We studied how the frequency of extreme winds is synchronised across land areas in the NH. To do this, we used a storm index based on unusually strong wind days, calculated from ERA5 climate data between 1940 and 2023. By applying a statistical method called principal component analysis (PCA), we found a major pattern; storminess in northern regions (above 50°N, like Europe and Asia) tends to rise and fall together, but in the opposite direction to more southern areas.

https://doi.org/10.5194/egusphere-2026-523
Preprint. Discussion started: 6 February 2026

We looked at how this storm pattern connects to global climate patterns of atmospheric surface temperature, sea surface temperatures and atmospheric pressure. These links suggest that known climate systems, such as the North Atlantic Oscillation, play a role in shaping storm behaviour. To test whether these climate features can actually cause storm changes, we ran experiments using a climate emulator model (ACE2). The model confirmed our findings and showed that temperature differences across the Earth's surface can trigger shifts in the jet stream, which, in turn, affect storm patterns. Overall, our research connects statistical patterns in storminess to physical climate processes, helping us understand how storm risks across continents may respond to global temperature changes.

https://doi.org/10.5194/egusphere-2026-523
Preprint. Discussion started: 6 February 2026

1 Introduction

Climate modes, such as the North Atlantic Oscillation (NAO), the Pacific-North American Mode (PNA), the Arctic and Antarctic Oscillation (AO and AAO), have been linked to large parts of the variability in (extratropical) atmospheric circulation and have been subjected to considerable scrutiny in terms of the mechanisms behind these climate modes and their potential predictability. Many climate modes are associated with surface temperature and precipitation anomalies. For instance, a stronger expression of the NAO during a particular boreal winter is linked to milder surface temperatures over Northern Europe (Rousi et al., 2020) and drier winters in the Western Mediterranean basin (Seager et al., 2020). Therefore, seasonal predictions of any of those climate modes would help improve seasonal forecasts across many regions of the world simultaneously. The NAO has been the target of many predictability studies with lead times ranging from months to years (Scaife et al., 2014; Athanasiadis et al., 2020), targeting the Tropical sea-surface-temperatures in the Pacific (Lim et al., 2019) and the Atlantic (Wang et al., 2004; Wu et al., 2024) oceans, sea-ice cover (Delworth et al., 2016), solar irradiance (Behr, 2022), volcanic eruptions (Dogar et al., 2024), etc.

In this study, we explore a related but distinct research question; whether or not coherent patterns of the frequency of weather extremes also exist. For the sake of clarity and focusing on wind extremes, this question translates to whether or not 'stormy' seasons (a higher frequency of daily wind extremes or more intense wind extremes) tend to appear simultaneously in different regions of the world, or whether stormy seasons in some regions tend to coincide with calmer seasons in other areas. The identification of those spatially coherent patterns could help disentangle the large-scale mechanisms (surface forcing or slowly varying large-scale atmospheric modes) behind seasons with more or less weather extremes and possibly also aid their seasonal prediction. In this paper, we focus on daily wind extremes, but the methodology can be applied to other types of daily-scale weather extremes.

This study also aims to statistically identify the potential drivers of those large-scale wind extremes modes, in particular, seasonal patterns of sea-surface temperature anomalies. Arising statistical relationships should ideally be confirmed by targeted simulations with global atmospheric models driven at the lower boundary by the identified SST anomaly patterns. For this purpose, we use a machine-learning atmospheric emulator, ACE2 (Watt-Meyer et al., 2025), instead of a full-fledged General Circulation Model. The ACE2 emulator has been trained with ERA5 data over the past 70 years (see Section 7). The advantage of using an emulator is its inference speed, which allows running a large number of simulations with different boundary surface conditions, and it may be closer to capturing the relationships between boundary forcing and atmospheric circulation than a GCM, which, in principle, may be burdened by model biases. On the other hand, the ACE2 emulator, based on a machine-learning model, essentially replicates the connections between boundary conditions and atmospheric circulation as found in the ERA5 data. This can introduce a degree of circularity, since the ACE2 emulator essentially exploits, albeit in a rather sophisticated manner, the statistical links between the different climate variables in the reanalysis. However, the ACE2 emulator is trained on high-resolution (6-hourly) reanalysis data (Watt-Meyer et al., 2025) and is therefore geared towards replicating those very short-term empirical links. Our statistical analysis, by contrast, is set up to identify statistical links between seasonal fields, sometimes including time lags over several seasons.

https://doi.org/10.5194/egusphere-2026-523
Preprint. Discussion started: 6 February 2026

In addition, to the tests of Watt-Meyer et al. (2025) we have subjected the ACE2 emulator to a basic test to ensure that it can generally replicate some of the patterns of seasonal atmospheric variability and the teleconnections of those patterns to surface mean seasonal climate anomalies, and that it can reproduce the statistics of wind extremes as in the training data set.

Wind extremes linked to tropical and Extra Tropical Cyclones (ETC) are one of the major natural hazards to society, leading to loss of human life and damage to infrastructure and the economy (von Storch et al., 2024; Sinclair et al., 2020; World Meteorological Organization, 2025). While the vast majority of cyclones occur over the oceans (Gray et al., 2024), resulting in more energetic waves and storm surges at the coasts, they can also be responsible for extensive damage on land, especially if they are associated with heavy precipitation (Hawcroft et al., 2012; Pfahl and Wernli, 2012; von Storch et al., 2024). Beyond their short-term weather-scale predictions, the long-term variability and possible long-term trends associated with climate change have been the focus of extensive research across different regions of the Earth (Gulev et al., 2001; Wang et al., 2006; Ulbrich et al., 2009; Shaw et al., 2016; Priestley and Catto, 2022; Crawford et al., 2023). The number and intensity of cyclones vary on decadal scales, possibly driven by climate modes such as the NAO (Gulev et al., 2001; Wang et al., 2006; Delworth et al., 2016; Zeng et al., 2019).

Types of wind extremes are distinguished by their spatial location and energy source (von Storch et al., 2024). The most prominent distinction made is between Tropical Cyclones that typically arise in the region 23.5°S–23.5°N and ETC originating in regions poleward of 35° latitude (von Storch et al., 2024; Lodise et al., 2022). Both types of cyclones are initiated and driven by baroclinic instabilities, i.e. temperature and pressure gradients in the atmosphere (McDonald, 2011; Shaw et al., 2016; Feser, 2018; Lodise et al., 2022; von Storch et al., 2024). ETC mainly arise in the boreal winter, due to a strong land-sea temperature gradient, because land cools faster than water (von Storch et al., 2021). This gradient is balanced through the ETC development and its associated heat transport (von Storch et al., 2021, 2024). Shaw et al. (2016) state that processes that alter temperature and pressure gradients, such as natural climate variability (climate modes) and anthropogenic forcing (through a warming climate), influence the variability of wind extremes.

Climate modes and their indices are useful precursors of wind characteristics, even on seasonal timescales (Merryfield et al., 2020; Laurila et al., 2021), and have been extensively studied. For instance, in the Northern Hemisphere (NH) wind speeds are influenced by the NAO, Atlantic Meridional Overturning Circulation (AMOC) and AO (Lodise et al., 2022; Feser, 2018; Ulbrich et al., 2009). Wang et al. (2006) studied the climatology of ETC activity and noted their natural decadal variability connected to the NAO and ENSO. Zeng et al. (2019) show that the NAO and Pacific Decadal Oscillation (PDO) are associated to positive wind speed anomalies on decadal timescales. Gulev et al. (2001) studied modes of variability of storm intensity using a Principal Component Analysis (PCA) and found a positive correlation with the NAO and PNA. Global climate modes, the NAO, ENSO, PNA and AMV, have also been found to be linked to compound wind and precipitation extremes (François et al., 2025).

The position of the jet stream also influences changes in wind speed and extremes (Schultz et al., 2019; Laurila et al., 2021) and its strength and position are linked to climate modes (Woollings et al., 2010). For example, Delworth et al. (2016) show that a positive NAO phase (strong pressure gradient between Iceland and the Azores) enhance the westerly windflows strengthening the jet stream. This is in agreement with the findings of Lodise et al. (2022), showing that a stronger NAO

https://doi.org/10.5194/egusphere-2026-523
Preprint. Discussion started: 6 February 2026

correlates with faster-moving ETC of stronger intensities along with a basin-wide northeast shift in cyclone centre density in the North Atlantic. Conversely, a weaker NAO is associated with a weaker and more meandering jet stream, which blocks the ETC from travelling towards Western Europe.

Unfortunately, wind extremes are often under-represented in common prediction schemes such as dynamical and statistical models (Schultz et al., 2019). Whereas dynamical models are based on the global circulation of the atmosphere and oceans, statistical models infer predictive skill from favourable climatic conditions and established teleconnections affecting the wind extremes (Klotzbach et al., 2019; Pfleiderer et al., 2020). To improve these prediction schemes, we need a better understanding of the relationship between wind extremes and their favourable climatic conditions (Intergovernmental Panel on Climate Change (IPCC), 2014; Priestley and Catto, 2022).

While a vast literature exists on the storm tracks of ETC and wind speed characteristics in the NH as well as their connection to climate modes or other large-scale meteorological patterns (Eichler and Higgins, 2006; Woollings et al., 2010; McDonald, 2011; Delworth et al., 2016; Shaw et al., 2016; Laurila et al., 2021; Bouwer et al., 2022), an analysis of the synchrony of land-regions with respect to the variability of wind extremes is, to our knowledge, missing. An understanding of co-varying land-regions regarding wind extremes can guide policy making and distribution of financial aid resources by informing on exposure. For example, regions with similar exposure to wind extremes could adopt comparable policies and infrastructure design. Additionally, regions with similar extreme wind variability may experience comparable shifts due to climate change.

We focus on these gaps by identifying regions with similar variability of wind extremes using a PCA of a predefined storm index based on grid-point exceedances of the 95th-Percentile of 10m surface wind speeds over land-regions in the NH for the extended winter season (ONDJFM) between 1940 and 2023 based on ERA5 reanalysis data (Hersbach et al., 2020). We investigate dynamical drivers of the wind extreme synchrony in two ways. First, we correlate climate fields of SST, MSLP and Skin Temperature (SKT, as the temperature of the surface at radiative equilibrium) with the timeseries of the storm index to obtain a predictive signal. Secondly, we construct a factual and counterfactual climate using the climate emulator ACE2 (Watt-Meyer et al., 2025) with artificial forcings obtained from the previous correlation analysis of SKT. We then diagnose changes in the wind extremes between the counterfactual and factual world to infer causal relationship between the SKT and the excited extremes.

This study advances understanding of the synchrony of regional wind extremes and their sensitivity to surface-temperature perturbations. It adds knowledge on the connection between large-scale drivers and regional extremes, which can improve predictive models and provides useful information for adaptation and mitigation planning, risk management and early warning systems.

The paper is structured as follows: We first introduce the datasets used to derive the storm index, which serves as a proxy for wind extremes. We then apply a PCA to the storm index to obtain regions of synchronised variability regarding wind extremes and their temporal excitement. Next, anomalies in possible physical drivers of storm variability are correlated with the PCA results to obtain a predictive signal. Using the ACE2 climate emulator, we conduct a sensitivity analysis using the predictive signal of SKT to construct a counterfactual climate and diagnose its differences in storminess relative to the factual world. We conclude by relating our results to the contemporary literature.

https://doi.org/10.5194/egusphere-2026-523
Preprint. Discussion started: 6 February 2026

2 Data

2.1 ERA5 reanalysis data

We use spatially resolved fields of variables such a zonal and meridional 10m surface wind, MSLP, SST and SKT from the European Re-Analysis 5 (ERA5) data provided by the ECMWF. The ERA5 dataset ranges from January 1940 to the present with daily estimates of atmospheric variables and is spatially resolved on a grid of approximately 0.25 degrees covering the Earth and is documented in (Hersbach et al., 2020). All variables are from the period from 1940 to 2023, with a global coverage. We use ERA5 data because it offers several advantages over other datasets (such as NCEP-Reanalysis), including higher spatial and temporal resolution, more recent updates, and improved data assimilation techniques.

2.2 ERA5 landmask

The ERA5 land-sea-mask provides a parameter indicating the proportion of land relative to ocean or inland waters (lakes, reservoirs, rivers, and coastal waters). The parameter ranges between zero and one and values above 0.5 can be comprised of a mixture of land and inland water but not ocean. Since we focus on land regions of the NH we select only those grid points where the land-sea-mask values are strictly above 0.5 for the development of the storm index.

2.3 NAO-Index

The NAO is a climate mode over the North Atlantic Ocean indicated by differences in MSLP between the Icelandic Low and the Azores High. We downloaded the NAO-Index from the NOAA database. They obtain the NAO index by applying a PCA on the daily anomalies 500 millibar height field over 0-90°N. For further information, we refer to the website of NOAA (National Centers for Environmental Information (NCEI), 2025).

3 Developing a percentile-based storm index

There are different approaches and metrics for measuring and quantifying storms, such as wind speed, vorticity, low (mean) sea level pressure and pressure gradients (Ulbrich et al., 2009; Feser, 2018; Priestley and Catto, 2022; Lodise et al., 2022; Crawford et al., 2023). Priestley and Catto (2022) show that results of the intensity of storms are independent of these metrics. Hence, it is sufficient to focus on one metric only. For the purpose of this study, we will use 10m surface wind speed as a metric to define wind extremes.

In general, one can distinguish two approaches for defining an index that counts occurrences of extreme wind speeds; absolute and relative threshold indices. Absolute threshold indices define extremes by exceedances of a fixed threshold. This is useful for regional impact analysis of extreme events (Zhang et al., 2011; Sillmann et al., 2013), where the relation between the imposed threshold and local damages is known. These indices are not useful for regional comparisons of wind extremes, as a fixed threshold does not account for local differences in wind speed (Zhang et al., 2011).

https://doi.org/10.5194/egusphere-2026-523
Preprint. Discussion started: 6 February 2026

In contrast, relative threshold indices define extreme events with respect to the local climatology. Hence, the definition of a wind extreme event is linked to the predominant local wind speeds. For example, in a region of mean wind speeds of around 3 m/s a wind speed of 8 m/s can already be considered extreme and unusual for that region, while a similar wind speed is considered as mild wind in a region that experiences average wind speeds of 12 m/s. Locally defined wind extremes enable better-targeted warnings and preparedness measures as well as more accurate planning for disaster response tailored to regional needs as communities and their infrastructure are adapted to their local climate and are sensitive to deviations. Since we aim to identify regions with similar variability around extreme wind events, we will use a relative threshold index. We define wind extremes by the exceedance of the local 95th percentile of detrended wind speed anomalies at the near-surface level.

3.1 Detrended wind speed anomalies

We compute the 10m surface wind speed based on zonal and meridional 10m winds (U and V) from the ERA5 dataset with daily time resolution on a global grid. At each grid-point (λ, ϕ) and time t we compute the 10m wind speed W as

$$W(t,\lambda,\phi) = \sqrt{U(t,\lambda,\phi)^2 + V(t,\lambda,\phi)^2}. \tag{1}$$

We neglect the seasonality of the wind speed data by computing monthly anomalies relative to the reference period 1940-2008. Having machine learning purposes in mind, we choose this reference period as it divides the total period from 1940 to 2023 into a calibration period (e.g. the reference period from 1940-2008) and a validation period (e.g. the remaining period from 2009-2023).

Let $\bar{W}_j(t,\lambda,\phi)$ be the mean wind speed of month j over the reference period at grid-cell (λ, ϕ), then

$$A(t,\lambda,\phi) = W(t,\lambda,\phi) - \bar{W}_{m(t)}(t,\lambda,\phi),$$

defines the daily anomalies at each grid-cell, where $m(t)$ is a function that returns the corresponding month of any given day t.

Since we want to focus on climate variability, we further detrend A by subtracting its linear trend A' at each grid cell. Note that we fitted the trend A' to the reference period 1940-2008 and extrapolated it to the remaining period 2009-2023. We did this in order to avoid data leakage in case we wanted to use these datasets for machine learning purposes. In machine learning, it is common practice to apply the statistics derived from the calibration set to the validation set to avoid data leakage.

Due to increased computing speed, we compute the linear trend by averaging the daily anomalies A to monthly anomalies $\bar{A}$. We then fit a first-order polynomial to $\bar{A}$ at each grid-cell resembling the trend. The monthly trend is then interpolated to a daily trend again by using the monthly slope and intercept resulting in $A'(t,\lambda,\phi)$. Finally, we subtract the daily trend from the daily wind speed anomalies at each grid-cell leading to the detrended daily anomalies

$$\tilde{A}(t,\lambda,\phi) = A(t,\lambda,\phi) - A'(t,\lambda,\phi).$$

https://doi.org/10.5194/egusphere-2026-523
Preprint. Discussion started: 6 February 2026

3.2 Percentiles of detrended anomalies

Since we use a percentile index for counting extreme wind events, we compute the 95th-Percentile of the detrended anomalies $\tilde{A}$ at each grid-cell. The computation of percentiles is based on the reference period 1940-2008. To exclude seasonality in wind speeds, we group percentiles by month. Hence, we obtain 12 maps of global wind speed percentiles $P_j(\lambda, \phi)$, one map for each month j of the calendar year.

3.3 Developing the storm index

We develop a storm index S by comparing the daily detrended anomalies $\tilde{A}$ to their respective percentile P_j and encode every timestep exceeding the percentile as 1 and all others as 0, i.e.

$$\mathrm{S(t,}\ \lambda, \phi) = \begin{cases} 1, & \text{for } \tilde{A}(t, \lambda, \phi) > P_{m(t)}(\lambda, \phi) \\ 0, & \text{for } \tilde{A}(t, \lambda, \phi) \leq P_{m(t)}(\lambda, \phi). \end{cases} \tag{2}$$

We further aggregated the daily index S to a monthly index $\bar{S}$ by summing over all days within a month $j(y)$ of year y, i.e.

$$\bar{S}(j(y), \lambda, \phi) = \sum_{t \in j(y)} S(t, \lambda, \phi). \tag{3}$$

Figure 1 shows the storm index $\bar{S}(\text{01-1979}, \lambda, \phi)$ for January in 1979 over the NH restricted to land-masses only.

https://doi.org/10.5194/egusphere-2026-523
Preprint. Discussion started: 6 February 2026

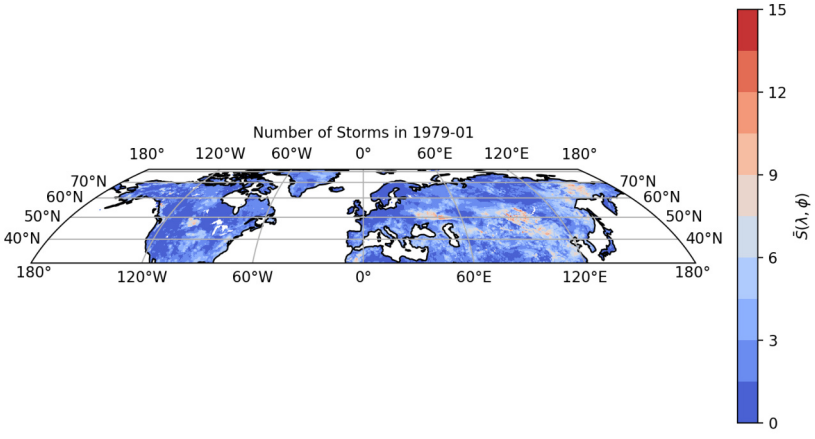

Figure 1. Storm Index $\bar{S}$ for January 1979 in the NH over land.

https://doi.org/10.5194/egusphere-2026-523
Preprint. Discussion started: 6 February 2026

4 PCA of the storm index

We use PCA of the storm index $\bar{S}$ to distangle the temporal and spatial variability of wind extremes. A theoretical description of the PCA can be found in Hsieh (2023) within the context of climate science. We briefly summarise the most important concepts, as the terminology will be used later on throughout the paper.

The overall idea of a PCA is to project the given n-dimensional data onto a single line (i.e. reducing the dimensionality of the data), while conserving as much variance of the data as possible. This involves a computation of the associated covariance matrix. The Eigenvalues μ_i and Eigenvectors e_i of that matrix are obtained and inform on the variability of the original data. The index i is called the mode of variability. Usually, the modes are ordered by decreasing amount of explained variance, which is the relative contribution $\tilde{\mu}_i = \mu_i / \sum_i^n \mu_i$ of one Eigenvalue to the total importance of the Eigenvectors. Ideally the explained variance $\tilde{\mu}_i$ is high for the first modes, indicating that most of the variance of the original data is captured in those modes. Depending on the desired amount of variance to retain, a subset of the first modes of the PCA is chosen. The Eigenvectors e_i are also denoted loading of the i-th mode. One can project, at each time step, the original input data of the PCA onto the eigenvectors e_i to obtain the scores a_i of the i-th principal component at that time step.

In this study, we apply the PCA to the storm index $\bar{S}$. This allows us to focus on the large-scale variability of wind extremes, where the first few modes likely represent physically meaningful storm patterns. We apply the PCA over the temporal dimension of the storm index, resulting in scores a_i, which represent the temporal variability of the storm index and hence the storm activity. The loadings e_i show the spatial variability associated to each a_i. We use the loadings to visualise regions that are synchronised with respect to wind extremes (i.e. regions that tend to evolve synchronously with respect to the storm index).

Let $S(t, \lambda, \phi)$ be the data we want to analyse, i.e. the storm index on a prespecified spatial and temporal domain. Before applying the PCA we standardize S to unit variance and mean zero at each grid-cell, resulting in S'. We then weight the data by the size of a grid-cell, i.e.

$$\tilde{S}(t, \lambda, \phi) = S'(t, \lambda, \phi) w(\lambda, \phi),$$

with $w(\lambda, \phi) = \sqrt{\cos(\phi)}$. We introduce the $\sqrt{}$ into the weighting because during PCA the variance is computed, i.e. a quadratic function is applied to $\tilde{S}$. Thus w effectively weights the storm index with the $\cos(\phi)$.

We then perform the PCA on $\tilde{S}$ along the time dimension t resulting in the scores $a_i(t)$ being timeseries and the loadings $e_i(\lambda, \phi)$ being spatial patterns associated to the i-th mode. Finally, we will apply Hotellings Original Scaling to the scores and loadings, leading to

$$\hat{a}_i = \frac{1}{\sqrt{\mu_i}} a_i$$

and

$$\hat{e}_i = \sqrt{\mu_j}\, e_i.$$

This ensures that all scores have unit variance (as $\mu_i = \mathbb{V}(a_i)$), which is needed to intercompare the plots of the scores amongst all modes. Additionally this ensures that the variance of the data $\tilde{S}$ is contained in $\hat{e}_i$. Since $\tilde{S}$ has mean zero and unit variance, before applying the PCA we can interpret the entries of $\hat{e}_i$ as the correlation between the score $\hat{a}_i$ and the storm index, i.e.

https://doi.org/10.5194/egusphere-2026-523
Preprint. Discussion started: 6 February 2026

$$\text{Corr}(\hat{a}_i(t), \tilde{S}_l(t)) = \hat{e}_{il}$$

where $\hat{e}_{il}$ is the l-th entry of the i-th loading.

Having machine learning purposes in mind, we applied the PCA to the reference period of 1940-2008 to compute $\hat{e}_{i,\text{1940-2008}}$ and $\hat{a}_{i,\text{1940-2008}}$, similar to the wind speed anomalies. We then standardise the storm index data $S_{\text{2009-2024}}$ with the mean and standard deviation of the $S_{\text{1940-2008}}$ and weight the data with w as described above. Note that this analysis shows storm variability rather than storm occurrence at specific grid points.

4.1 PCA of the landmasked storm index in the NH

Through the course of this study we applied a PCA over several spatial and temporal subdomains of the storm index. Since the initial goal was to find regions that are of synchronised behaviour with respect to storms on a global scale, we applied the PCA to $\bar{S}$ defined on a global grid with monthly resolution as described in Equation 3. Unfortunately, the explained variance of the first five modes was low (e.g. $\sum_{i=1}^{5} \tilde{\mu}_i < 8\%$, with $\tilde{\mu}_1 \approx 2\%$).

Hence, we decreased the region analysed, keeping it as large as possible but making it as small as necessary to increase the explained variance $\tilde{\mu}_i$. Finally, we obtained an explained variance of $\tilde{\mu}_1 \approx 8\%$ for the first mode when restricting the analysis of the storm index to landmasses in the NH defined by the ERA5 landmask and all latitudes north of 30°N (see Fig. 1) and aggregating it to the extended winter season ONDJFM. Hence, for the period 1940-2008 we end up with a total of 69 winter seasons (e.g. timesteps). It is further noted that the second mode explains 5.8% of the variability, and that the first five modes explain $\sum_{i=1}^{5} \mu_i \approx 24\%$ of the variance in the storm index. A cumulative explained variance of 90% is obtained when using the first 52 modes.

These results already show that the global synchrony of storminess is low, at least within the linear character of the inter-regional links assumed by the PCA. Only after restricting the PCA to smaller continental sub-global regions does it identify modes that can account for a sizeable portion of the total variance. This is already in contrast with similar analysis of global or hemispheric PCA of seasonal means of sea-level pressure, which do show large-scale modes, e.g. the Arctic Oscillation, the Antarctic Oscillation, the Pacific North American Pattern, that explain a large portion of the total variance.

We focused on the first mode of the PCA of the storm index explaining the largest contribution to the variability of wind extremes. The corresponding score $a_1(t)$ (temporal variability) and its loading pattern $e_1(\lambda, \phi)$ (spatial variability) are shown in Fig. 2.

https://doi.org/10.5194/egusphere-2026-523
Preprint. Discussion started: 6 February 2026

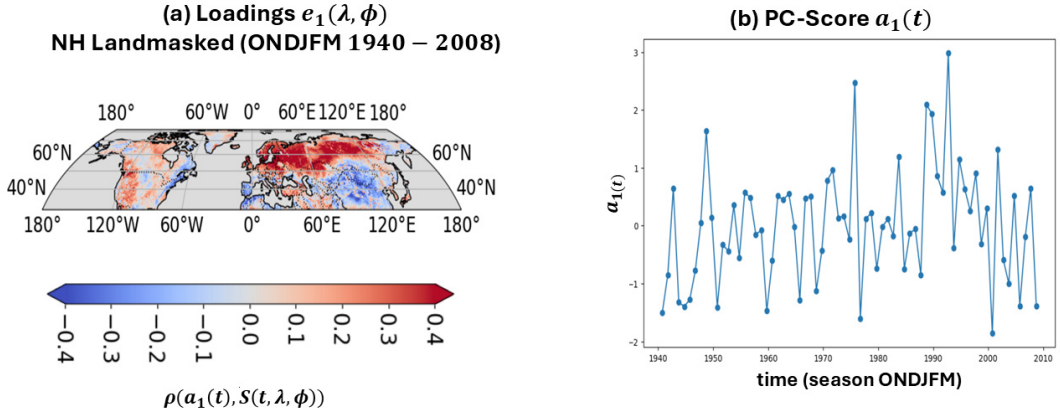

Figure 2. Results of the first mode of a PCA applied to the storm index $S(t, \lambda, \phi)$, which is restricted to the NH land-regions aggregated over the extended winter season ONDJFM from 1940-2008. (a) Loadings $e_1(\lambda, \phi)$ show the spatial variability of the storm index and (b) shows the score $a_1(t)$, i.e. the temporal variability of the storm index. Hotellings Scaling was applied, such that e_1 shows the correlation between the temporal variability a_1 of the index and the storm index S itself.

https://doi.org/10.5194/egusphere-2026-523
Preprint. Discussion started: 6 February 2026

Since we scaled the a_1 and the e_1 using the Hotelling´s scaling, the loadings e_1 show the correlation between a_1 and the standardised storm index. Hence, in Fig. 2 red (blue) regions can be interpreted as higher-than-normal (lower-than-normal) extreme winds if $a_1(t) > 0$ and vice versa if $a_1(t) < 0$. Regions with similar loading values indicate where variability is clustered and the same underlying physical dynamics might influence them. Additionally, red and blue regions display opposite phases, meaning that high storm variability in one region is associated with low storm variability in the other, and vice versa.

Looking at the temporal variability of the index in Fig. 2 we identify two highest peaks of a_1 in the seasons 1976/1977 and 1993/1994 and the two lowest troughs in 1977/1978 and 2001/2002, corresponding to high storm variability in red and blue regions of e_1, respectively.

From Fig. 2 we can see a clear north-south clustering of regions that are synchronised with respect to the variability of the index. The separation appears north and south of the 50°N latitude within Europe and Asia. This suggests that regions such as Germany, the UK, Scandinavia and Russia (red regions) are subject to similar storm variability, which tends to have the opposite phase in France, Italy, Spain, Portugal, Morocco and large parts of Asia south of 50°N (blue regions).

To verify the robustness of the loading pattern in Fig. 2, we analysed the months of the storm season separately by aggregating the index over each month in ONDJFM in isolation. We then applied a PCA to the timeseries of the storm index that consists only of the information of a single month. This analysis resolves the pattern in Fig. 2 of the seasonal aggregates into monthly structures. The pattern of e_1 reappeared across all months of the storm season, verifying its robustness (not shown).

5 Relating physical drivers to the storm variability

We correlate detrended anomalies of SST, MSLP and SKT climate fields with the score $a_1(t)$ of the first principal component to identify a predictive signal in the predictors. The detrended anomalies were computed similarly to the wind speed anomalies in Section 3.1, i.e. by subtracting monthly climatologies of the reference period of 1940-2008 and then linearly detrending the anomalies over the whole timeperiod 1940-2023 based on the extrapolated linear trend of the reference period.

To identify a prognostic relationship between the detrended anomalies and storminess in the ONDJFM months, as captured by $a_1(t)$, we separately correlate them with each one of the previous months from January to September. For instance, the SST anomalies of January 1979 are temporally aligned with the PCA-Score of the storm season in 1979/1980. This analysis results in a total of nine correlation maps, one for each month between January to September.

We do not show and discuss the correlation of SKT here but discuss it later during the sensitivity analysis in Section 8.2.

5.1 Correlation between SST & a_1

The Pearson correlation of detrended SST anomalies with a_1 for the leading months Jan-Sep is depicted in Fig. 3. One can see an emerging signal in the Central and Eastern Pacific as well as in the North Atlantic (negative correlations). The signal strength increases as the predictor month approaches the storm season ONDJFM. In the North Atlantic, the signal is robust and persists across all lead times, whereas in the Pacific it becomes robust only from May onward.

https://doi.org/10.5194/egusphere-2026-523
Preprint. Discussion started: 6 February 2026

The negative correlation to the Pacific Ocean suggests an influence of the ENSO climate mode. Warmer (colder) SSTs are associated with lower (higher) values a_1 and hence more frequent storminess in the negative (positive) regions of the pattern e_1. The signal in the Northern Atlantic could be connected to the AMOC and its heat transport, especially in the region of the Gulf Stream. Again, warmer SST in the North Atlantic is connected to lower a_1 and hence more frequent storminess in the negative regions of e_1.

One possible explanation of this signal might lie in a stronger baroclinic instability in the North Atlantic Atmosphere driven by an increase in atmospheric temperature gradients due to changes in SST. Another possibility might be the influence of the AMOC on the Jet-Stream position, since a weaker AMOC has been found to be connected to a poleward shift of the mid-latitude jets (Bellomo et al., 2021).

https://doi.org/10.5194/egusphere-2026-523
Preprint. Discussion started: 6 February 2026

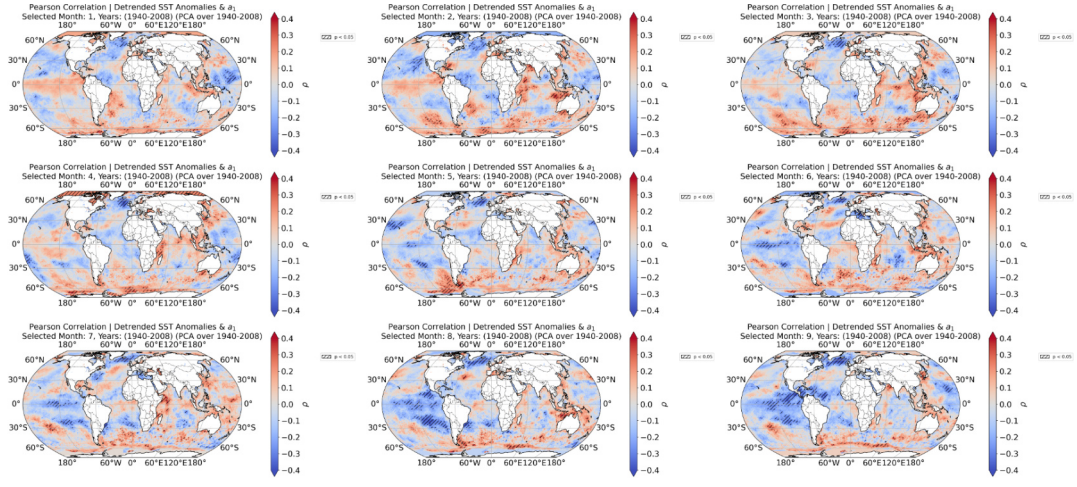

Figure 3. Pearson correlation of detrended anomalies of SST with PC-score a_1 for each month in Jan-Sep. Hatched lines show significance with p-value $p < 0.05$.

https://doi.org/10.5194/egusphere-2026-523
Preprint. Discussion started: 6 February 2026

5.2 Correlation between MSLP & a_1

The correlations between detrended anomalies of MSLP and a_1 are shown in Fig. 4. The correlation reveals a dipole pattern in the NH indicating a possible influence of MSLP gradients on the storm variability. Depending on the month used as a precursor, the gradient signal strength shifts zonally. For example, in January, the strongest dipole correlations are observed over Europe and Asia, whereas in August this signal shifts to the North Atlantic. The signal is in accordance with the pattern of the NAO, which reflects below-normal pressure across the high latitudes of the North Atlantic and above-normal pressure over the central North Atlantic during its positive phase (National Centers for Environmental Information (NCEI), 2025). To test this connection, we correlated the NAO-Index (see Section 2) aggregated over the ONDJFM and JJAS seasons with a_1 and obtained moderate positive correlations of 0.31 and 0.26, still significant at the 5% significance level. A stronger NAO tends to be hence associated with stronger a_1, e.g. more frequent storm activity north of 50°N (red regions in e_1).

https://doi.org/10.5194/egusphere-2026-523
Preprint. Discussion started: 6 February 2026

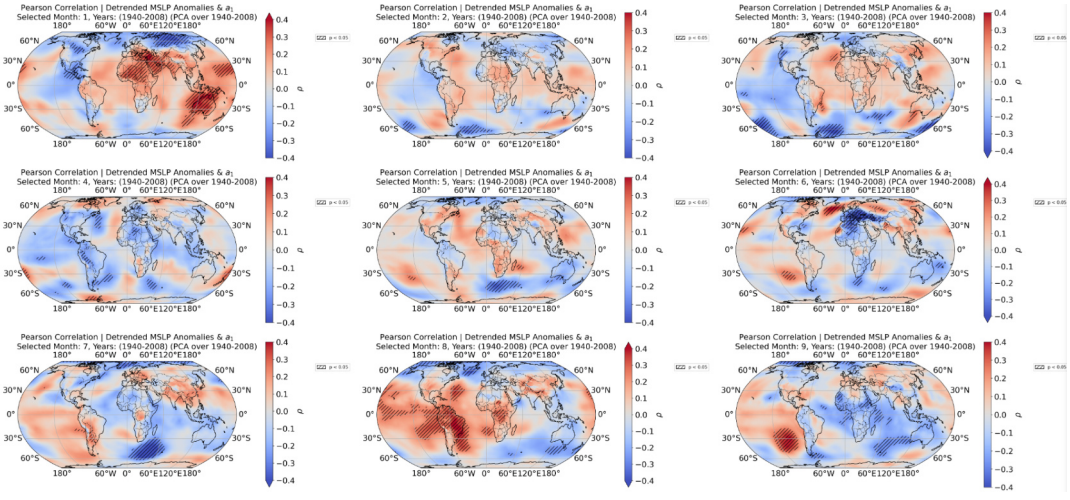

Figure 4. Pearson correlation of detrended anomalies of MSLP with PC-score a_1 for each month in Jan-Sep. Hatched lines show significance with $p < 0.05$.

https://doi.org/10.5194/egusphere-2026-523
Preprint. Discussion started: 6 February 2026

6 Testing simple prediction schemes

The signals obtained from the correlation analysis of anomalies in SST and MSLP with a_1 indicated that these variables are possibly useful predictors. Hence, we set up a handful of simple prediction schemes, ranging from linear regression to random forests, where a_1 is the dependent variable (predictand) and the anomalies of SST, MSLP and other unmentioned variables as well as indices of climate modes were used as independent variables (predictors). Despite the aforementioned correlations, these prediction schemes did not lead to useful predictive skill using as a metric the R^2-score. This motivated us to validate the choice of predictors and their derived signals by conducting simulations with the ACE2 emulator to ascertain the causal relationships with storm variability.

Before we apply the sensitivity analysis, we validate the statistics of ACE2 against the statistics of the ERA5 data for the investigated climate variables.

7 ACE2 climate emulator: Validation

The ACE2 Climate Emulator is a neural network containing 450M parameters trained to emulate atmospheric dynamics. It is driven by prescribed sea-surface-temperatures, solar irradiance, greenhouse gas concentrations, and sea-ice cover. It produces estimations of the most important atmospheric variables, including near-surface variables (precipitation, 2-meter air temperature, 10-meter wind, sea-level pressure) and variables at 8 tropospheric and lower stratospheric levels (meridional and zonal wind components, air temperature, specific humidity). It has been so far trained with two different data sets: the output of the FV3GFS the atmospheric component of the United States weather model, and the ERA5 reanalysis (Watt-Meyer et al., 2023, 2025). The temporal resolution is 6-hourly, simulating a decade in one hour of computing time on an NVIDIA A100-SXM4 GPU. ACE2 is, to our knowledge, the sole atmospheric emulator that runs stably for more than 6 months and can even support millennial-scale stable simulations (Watt-Meyer et al., 2025). In this study, we conducted numerous simulations with the ERA5-trained model for 70-year periods, varying initial conditions and sea-surface temperatures, without experiencing any instabilities.

A relevant characteristic is that the ACE2 emulator produces its own inter variability, in the same fashion as an atmospheric general circulation model does: it is a non-linear model that, when started from slightly different initial conditions produces system trajectories that immediately start diverging from one another. This results in unsynchronised variability that is not tied to the external forcing (daily and annual cycles or long-term anthropogenic trends). For example, the North Atlantic Oscillation index from a decadal-long simulation with ACE2 is uncorrelated with observations and with any twin simulation started from different initial conditions.

For a more in-depth description of these results, we refer to Watt-Meyer et al. (2023) and Watt-Meyer et al. (2025).

https://doi.org/10.5194/egusphere-2026-523
Preprint. Discussion started: 6 February 2026

7.1 Statistical comparison between ACE2 and ERA5

According to Watt-Meyer et al. (2025) ACE2 generates emergent phenomena such as tropical cyclones, sudden stratospheric warmings and accurately reproduces the atmospheric response to El Niño variability. We tailor a similar analysis to the realm of wind extremes in the NH by comparing various statistical components, such as the climatology of 10m surface windspeed, the spatial distribution of the 95th percentiles and peak over threshold counts, between the ACE2 simulation output and the ERA5 data. Additionally, we compare the representation of wind-extremes-related climate modes, namely the AO, the NAO and PNA, as well as the spatial footprints of their corresponding indices to the 10m surface windspeed (i.e. teleconnections).

7.1.1 Methods

For the comparison between ACE2 and ERA5 we use the initial conditions of 01.02.1940 (00:00.00 UTC) from ERA5 reanalysis and run a free simulation until the end of 2022 driven by the standard forcings obtained through downloading and installing ACE2, namely solar irradiance, sea-surface-temperature, sea-ice cover, and carbon dioxide atmospheric concentrations. We then analyse the period from 1941 to 2022 and resample the ACE2 output from 6H temporal resolution to daily timesteps on a 1° global grid. To match the grid-sizes, we linearly interpolate ERA5 data from the 0.25°-grid to the 1°-grid of ACE2. From the zonal and meridional wind-components, we compute the 10m surface wind speed as shown in Eq: 1. In addition to the 10m surface windspeed, we use the surface pressure (‘PRESsfc‘) for the comparison. As skill metrics, we compute the bias, the RMSE, the variance ratio and spatial Pearson correlations using ERA5 data as a reference.

7.1.2 Climatology and percentile of wind speed

ACE2 reproduces the seasonal climatology (DJF, MAM, JJA, SON) for 10m surface wind speed sufficiently well, with a spatial correlation of 0.99 and a negligible RMSE (not shown). The seasonal 95th-percentiles of ACE2 show reasonable similarity to the 95th-percentiles of the ERA5 data, again with a correlation of 0.99 (see Fig. 5). Even though RMSEs are generally small (approx. 0.5 m/s) it seems that ACE2 overestimates the percentiles in the JJA season within the North Western Pacific basin close to the typhoon-impacted region.

https://doi.org/10.5194/egusphere-2026-523
Preprint. Discussion started: 6 February 2026

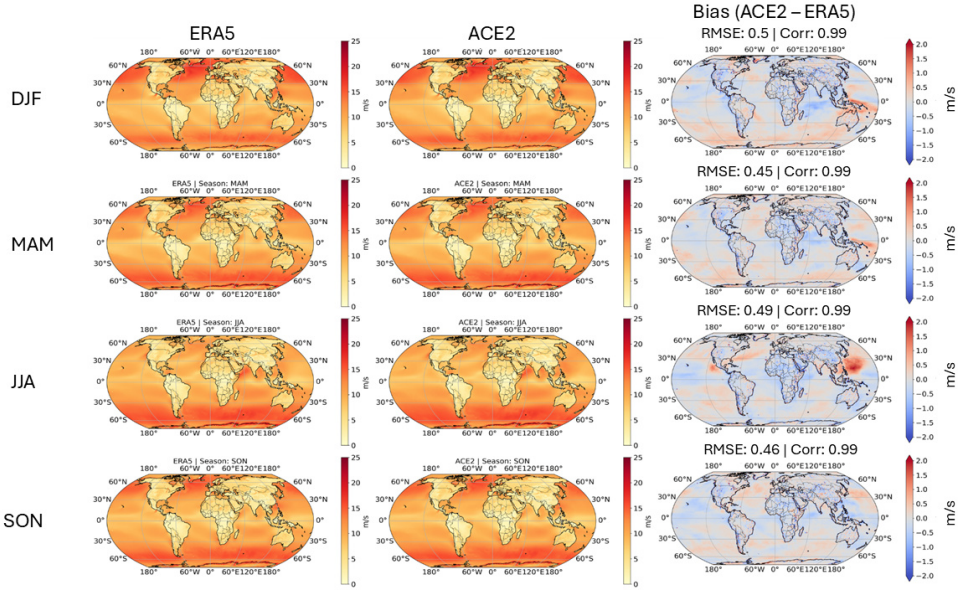

Figure 5. Seasonal 95th-Percentile (from top to bottom; DJF, MAM, JJA, SON) of the 10m surface wind speed in ERA5 (left), ACE2 (center) and its bias (right). Metrics of RMSE and correlation are stated in the title of the bias.

https://doi.org/10.5194/egusphere-2026-523
Preprint. Discussion started: 6 February 2026

7.1.3 Peak over Threshold (POT) of 10 m wind speed

We use monthly local 95th percentile (similar to $P_{m(t)}(\lambda, \phi)$ in Eq. 2) of the ERA5 daily-mean wind speed dataset as thresholds to compute daily exceedances (Peak over Threshold (POT)) for both datasets and aggregate the daily exceedances to seasonal exceedances (DJF, MAM, JJA, SON) by summation. We analysed the frequency and intensity of the exceedances in both datasets.

To analyze the frequency of POT-events (i.e. the number of threshold exceedances) we compute the global sum of seasonal exceedances for both datasets obtaining two timeseries as well as their ratio (ACE2 / ERA5), both shown in Fig. 6. The seasonal mean bias (ACE2 - ERA5) is at 20365 counts per season and the seasonal mean ratio at 1.07, indicating that ACE2 seems to overestimate the POT-events by around 7%.

Interestingly, both datasets show a similar long-term increasing trend in the frequency of POT-events. Since ACE2 is a free-running simulation starting in 1941, with no data assimilation, this trend in ACE2 can only be driven by external forcing. Hence, ACE2 has learned from the ERA5 data set that periods with stronger external and/or boundary forcing tend to witness stronger wind extremes. This is remarkable, as ACE2 is trained with high-frequency (6-hourly) data and uses only three time-variant forcing variables, e.g. solar irradiance, surface temperature and global mean CO_2 atmospheric concentration. Hence, the resulting trend is likely related to one or all of these forcing variables, suggesting a connection between anthropogenic forcing and an increase in global wind extremes.

To estimate the intensity of exceedances, we compute the amount by which the wind speed exceeds the ERA5 threshold at each grid cell and timestep, if the threshold is exceeded. We then average this excess exceedance quantity over all timesteps that exceed the threshold and denote it the mean exeedance intensity. ACE2 recovers the mean exceedance intensity well with a spatial correlation of 0.96 and a RMSE of 0.13 m/s (global mean exceedance intensity, not shown).

https://doi.org/10.5194/egusphere-2026-523
Preprint. Discussion started: 6 February 2026

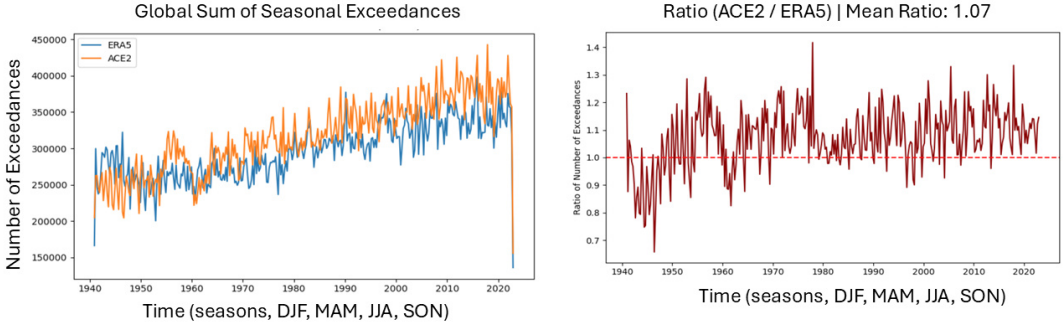

Figure 6. Left: Global sum of seasonal exceedances for ERA5 (blue) and ACE2 (orange) between 1941 and 2022. Right: Ratio (ACE2 / ERA5) of the global sum of seasonal exceedances.

https://doi.org/10.5194/egusphere-2026-523
Preprint. Discussion started: 6 February 2026

7.1.4 Climate modes and links between them

We compared several climate modes between ACE2 and ERA5, such as the Antarctic Oscillation (AO), North Atlantic Oscillation (NAO) and Pacific-North American Mode (PNA) as well as the link between the latter two.

We define all modes through the loadings of selected principal components of a PCA applied to monthly surface pressure anomalies between Jan-Dec in the period from 1941 to 2022 for selected regions and each dataset. The AO is the loading pattern of the first principal component of the PCA applied to the region 20°N-90°N across all longitudes, while the NAO-pattern is obtained by restricting the PCA to the region 20°N-90°N and 90°W-20°E. Usually, 500 mb height anomalies are used to compute the PNA-pattern, but we approximate it by applying a PCA to surface pressure anomalies within the region of 20°N-90°N and 120°E-60°W, from which the third component resembles the PNA-pattern.

The resulting loading patterns and metrics (explained variance and spatial correlation) are depicted in Fig. 7. ACE2 resembles the analysed climate modes sufficiently, showing a similar spatial structure as in the ERA5 dataset (spatial correlation of around 0.9) and a similar magnitude of the explained variance.

Additionally to the PCA, we also explore the connections between the NAO-Index and PNA-Index between both datasets. We computed a (normalized) NAO-index of monthly timestep by computing the differences between the average of the surface pressure anomalies over the Azores (35°N - 40°N, 25°W - 15°W) and Iceland boxes (60°N - 65°N, 25°W - 15°W) at each timestep and normalize it by the mean and standard deviation of either the ERA5 or ACE2 statistics. To approximate the PNA-index we use the score related to the loading pattern obtained from the PCA. For both indices, we compute again the correlation, variance ration, RMSE and bias between the indices based on the ERA5 and ACE2 datasets. We find that ACE2 generates NAO and PNA variability with realistic amplitudes (low bias and RMSE) but independent phases (low correlation). The latter is expected since ACE2 is a free-running simulation, and no synchrony with observations is to be expected.

We also analyse the NAO-PNA relationship within ACE2 compared to ERA5. We base our approach on a similar analysis done by Renggli et al. (2011), who analysed the relationship between NAO-PNA in the previous reanalysis ERA40 and in simulations with global climate models. We use the NAO-index and PNA-index as discussed before and construct a 21y centered rolling window starting in 1941 and ending in 2022 based on the monthly timesteps of the indices to compute the rolling correlation between both indices. The resulting correlation timeseries for both datasets and corresponding metrics are shown in Fig. 8.

The rolling correlation derived from ERA5 shows a multi-decadal coupling between the NAO and PNA with stronger phases in the 1940s and 1950s as well as 2020s and almost no coupling around the 1980s. ACE2 captures this relationship between NAO and PNA with a temporal correlation of approximately 0.7. Remarkably, even though it is a free-running simulation, it reproduces the multi-decadal coupling or lack thereof, seen in ERA5 data set. Again, the similar temporal evolution of the coupling between NAO and PNA not only validates the behaviour of the ACE2 emulator but also suggests that this coupling may be related to external forcing and/or boundary conditions.

https://doi.org/10.5194/egusphere-2026-523
Preprint. Discussion started: 6 February 2026

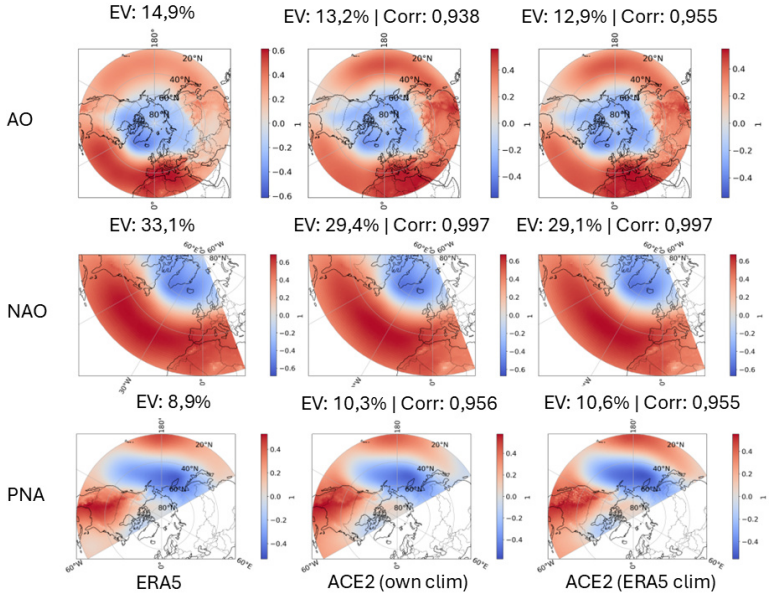

Figure 7. Climate modes, e.g. the AO (top), NAO (center) and PNA (bottom), defined by loading patterns of a PCA applied to surface pressure obtained from ERA5 (left), ACE2 with respect to its own statistics (center) and ACE2 with respect to the ERA5 statistics (right). Titles indicate the explained variance (EV) and the spatial correlation between the ERA5 and ACE2 patterns.

https://doi.org/10.5194/egusphere-2026-523
Preprint. Discussion started: 6 February 2026

	Correlation	VarianceRatio	RMSE	Bias
ACE2 (own climatology)	0.715	0.942	0.057	0.004
ACE2 (ERA5 climatology)	0.556	0.756	0.079	-0.043

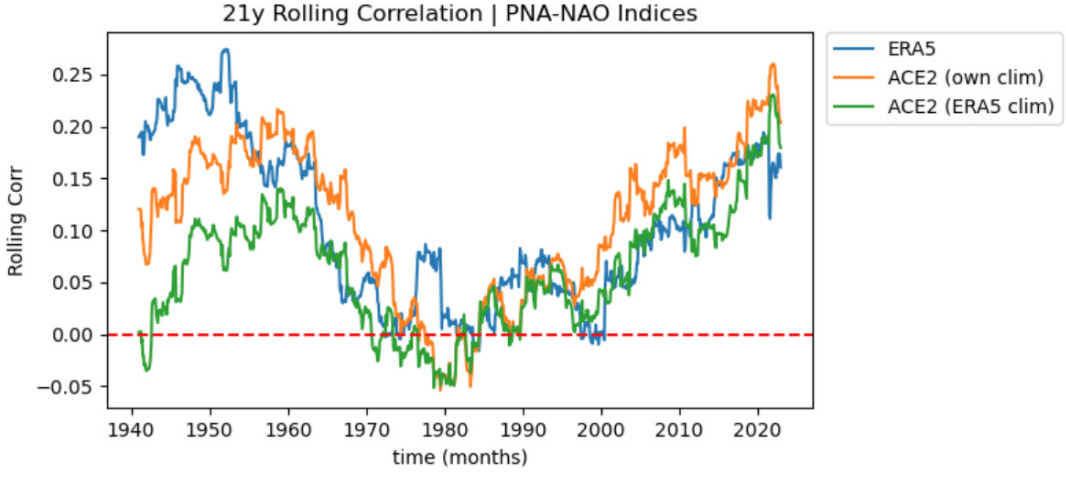

Figure 8. Timeseries of the Pearson correlation across a 21y rolling window between the NAO-index and PNA-index in the timeperiod 1941-2022 based on the reference ERA5 (blue), ACE2 based on its own statistics (orange) and ACE2 based on the ERA5 statistics (green). The table above shows metrics of ACE2 referenced to ERA5.

https://doi.org/10.5194/egusphere-2026-523
Preprint. Discussion started: 6 February 2026

7.1.5 Teleconnection patterns

To validate the links between the large-scale patterns of atmospheric variability to the surface winds, we correlate the NAO-index and PNA-index from Section 7.1.4 with the 10m wind speed at every grid-cell in the NH in ERA5 and in ACE2 (see Fig. 9). We computed two versions of each index, one normalised using ERA5 statistics (left and right columns of Fig. 9) and one normalised using ACE2 statistics.

ACE2 shows similar teleconnection patterns between the NAO-index and 10m wind speeds as ERA5 with a spatial correlation of 0.91. The teleconnection pattern also highlights expected regions in the Northern Atlantic, forming a tripole. The PNA-teleconnection pattern is also well reproduced , yet with lower spatial correlation of 0.78. It shows an expected tripole pattern in the Northern Pacific, which is indirectly driven by the surface pressure anomaly changes due to the PNA-mode. A visual comparison of the tripole-patterns indicates that in ACE2 the tripole-pattern is spread over a larger spatial domain compared to ERA5.

https://doi.org/10.5194/egusphere-2026-523
Preprint. Discussion started: 6 February 2026

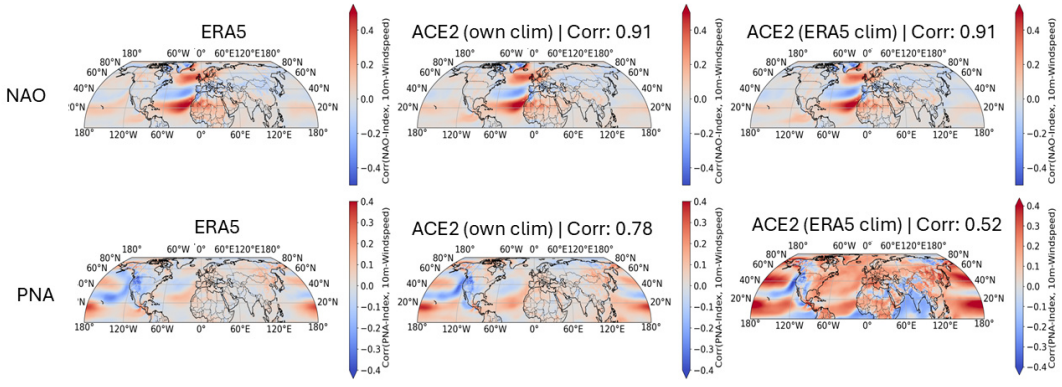

Figure 9. Teleconnection pattern between 10m wind speed in the Northern Hemisphere and the NAO-index (top) and PNA-index (bottom). Left: Wind speed and indices based on ERA5. Center: Wind speed and indices based on ACE2. Right: Wind speed based on ACE2 and indices based on ERA5 statistics. Titles indicate the spatial correlation between ACE2 and the reference ERA5.

https://doi.org/10.5194/egusphere-2026-523
Preprint. Discussion started: 6 February 2026

8 Sensitivity analysis based on the ACE2 emulator

In this section, we describe the results of the sensitivity simulations with ACE2 to changes in surface temperature. The purpuse of this analysis is to support the links between the anomalous boundary conditions and the frequency of wind extremes. Since the ACE2 only emulates the atmosphere dynamics, and not the oceans', it is not possible to force a simulation with the patterns of surface temperature in the months previous to the extended winter season, e.g., in April, and let the emulator simulate the evolution of atmosphere and of the boundary conditions through the next winter. For that type of simulation, we would need a full-fledged Earth System Model and conduct a standard initialised seasonal forecast simulation. Therefore, in this section, we limit ourselves to test whether the ACE 2 emulator simulates a change in the statistics of extreme winds during the extended winter seasons when driven by boundary conditions of the same winter season. Thus, this setup is not a predictive simulation, but just an analysis of sensitivity to changes in the surface boundary conditions.

We prescribe the SKT (see Section 8.2) in two distinct ensembles of the simulations of the extended winter season ONDJFM for each year in the period 1940 to 2022. Each one started on October 1st, 00 UCT. This results in a total of 83 simulations in each ensemble. Note that the last simulation starts on October 1st 2021, and covers the season 2021/2022. We cannot simulate 2023 because we only have forcing data through 2022.

The two ensembles differ in their boundary conditions as follows:

1. **Factual Climate:** We use the default (observed) boundary and initial conditions of the ACE2-emulator.
2. **Counterfactual Climate (stormy):** We prescribe the patterns of the boundary conditions based on correlation patterns between SKT and the PC-score a_1 as described in section 8.2, s.t. the storminess is expected to increase in the NH.

If the signal of the predictor used for the forcing of the counterfactual world is indeed connected to wind extremes, the statistics of the counterfactual scenario should deviate from the factual climate and show a higher frequency of extreme winds, especially in the indicated loading regions of e_1.

8.1 Initial conditions

The ACE2 emulator, as provided by its authors, only contains initial conditions for all time steps in five distinct years, 1940, 1950, 1979, 2000 and 2020. Since we want to start the simulation in October 1st of any given year between 1940 and 2022 we will apply the same initial conditions of October 1st 1940 to each simulation for the period 1940-1949; and similarly the initial condition of 1950 to the period of 1950-1978 and so on.

8.2 Boundary conditions (forcing)

We could identify an emerging signal between global SST and MSLP patterns and the storminess in the NH. Unfortunately, ACE2 does not use any of these variables as forcing variables, but the global spatially resolved SKT. Since SKT is indirectly related to SST and MSLP we will use it to alter the forcing in the counterfactual world.

https://doi.org/10.5194/egusphere-2026-523
Preprint. Discussion started: 6 February 2026

Similarly to the correlation analysis of SST and MSLP, we regress the spatially resolved fields of SKT on a_1, for each month in ONDJFM separately. This computation leads to 6 correlation maps, one for each month.

The resulting patterns M are shown in Fig. 10. A strong signal within the storm season ONDJFM is largely present over the NH, mainly with higher temperature over Asia. Depending on the month, there is a shifting zonal temperature gradient between Europe and Asia, most likely influencing atmospheric circulation. In the US and Canada, a temperature gradient is excited, increasing from north to south for the winter months, OND. This gradient shifts in spring and decreases from north to south.

https://doi.org/10.5194/egusphere-2026-523
Preprint. Discussion started: 6 February 2026

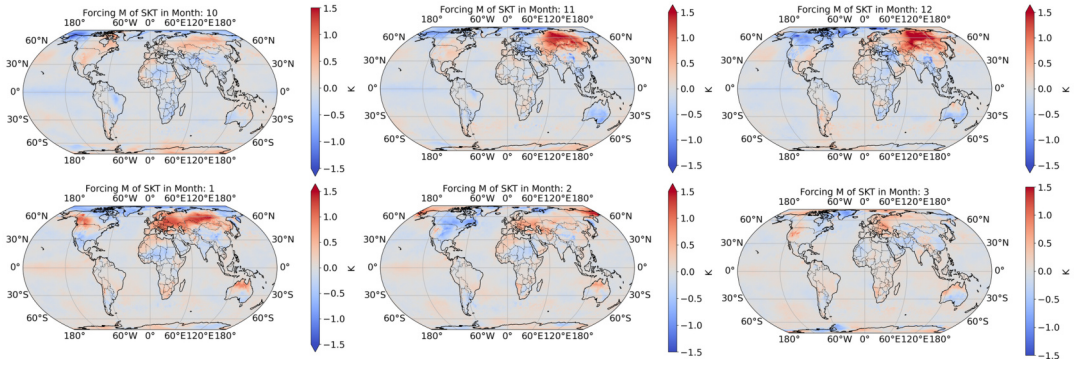

Figure 10. Pearson correlation of detrended anomalies of SKT with PC-score a_1 multiplied by the standard deviation of SKT for each month in OND (top row) JFM (bottom row). These fields are used as baseline boundary conditions for the ACE2 simulations.

https://doi.org/10.5194/egusphere-2026-523
Preprint. Discussion started: 6 February 2026

The ACE2 emulator expects a forcing variable with 6-hourly time resolution. We add the spatial patterns $M(j, \lambda, \phi)$ of month j to each 6-hourly timestep t of the forcing data $F(t, \lambda, \phi)$ of the factual world to generate the artificial forcing

$$\tilde{F}(t, \lambda, \phi) = F(t, \lambda, \phi) + c \cdot M(m(t), \lambda, \phi),$$

for the counterfactual simulation scenario. Here $m(t)$ maps the timestep t onto its corresponding month j. The factor c is used to amplify the signal M according to the simulation scenario (see the next subsection).

8.3 Simulation scenarios

We run the simulation for three different scenarios denoted as skt_1M, skt_2M, skt_3M, where the label indicates the amplification factor c. We amplify the artificial additional anomalies of SKT to analyse and demonstrate its effects and expect bigger differences in the statistics of the output variables between the factual and the counterfactual world with respect to storminess if we increase the amplification.

8.4 Output variables & their diagnostics

ACE2 provides multiple output variables, but we focus on those related to atmospheric wind speed at several vertical levels. The output variables used in this sensitivity analysis are

- *PRESsfc:* The atmospheric pressure at surface level
- *UGRD10m, VGRD10m:* The 10m-wind speed in east and northward direction
- *eastward_wind_5, northward_wind_5:* The 594 hPa east and northward wind speed referred here to as the wind speed at the 600 hPa level.
- *eastward_wind_3, northward_wind_3:* The 253 hPa east and northward wind speed referred here to as wind speeds at the 250 hPa level.

We apply the same diagnostics for each variable and scenario. Wind speeds are computed from the output variables if possible.
First, we compute the difference

$$\Delta(t, \lambda, \phi) = X_{\text{Counterfactual}}(t, \lambda, \phi) - X_{\text{Factual}}(t, \lambda, \phi) \tag{4}$$

between the output variable $X_{\text{Counterfactual}}$ of the counterfactual world and X_{Factual}, the output of the factual world at each timestep t and grid cell (λ, ϕ). To visualise this metric spatially, we compute the temporal mean as

$$\bar{\Delta}(\lambda, \phi) = 1/n_t \sum_t \Delta(t, \lambda, \phi),$$

where n_t is the number of timesteps.

https://doi.org/10.5194/egusphere-2026-523
Preprint. Discussion started: 6 February 2026

This metric shows how the counterfactual deviates spatially from the factual world during the ONDJFM season, providing insight into the possible influence of the altered surface-temperature forcing $\tilde{F}$.

We compute the wind speed of the factual and counterfactual worlds in order to compare their storm behaviour. We compute the local wind speed as $W(t,\lambda,\phi) = \sqrt{U(t,\lambda,\phi)^2 + V(t,\lambda,\phi)^2}$.

We denote the wind speed at three different levels of altitude depending on the output variable; they are the 10m surface wind (WSGRD10m), the wind speed at approx. 600 hPa (wind_speed_5) and the wind speed at approx. 250 hPa (wind_speed_3). First, we compute the temporal mean difference $\bar{\Delta}$ between the counterfactual and factual world, and also compare the differences in the respective daily 95th percentile to account for changes in wind extremes.

Lastly, we analyse the differences in wind speed between two composites of the PC-score $a_1(t)$.

8.4.1 Differences in mean pressure

The $\bar{\Delta}$ of the surface pressure between the counterfactual and factual worlds is depicted in Fig. 11. In the NH, especially in the Northern Atlantic, one can see a dipole pattern of the surface pressure. Higher pressure is observed in the counterfactual world between 60°W and 0° and north of 60°N in the North Atlantic, while pressure is lower in the same zonal region south of 60°N. This pattern is present for all amplitudes of the additional boundary conditions and strengthens as this amplitude increases. This reassures the statistical significance of the patterns. There is a strong similarity of these patterns to the NAO.

A consequence of this pattern is stronger pressure gradients, which in turn leads to a shift in zonal and meridional winds close to that region, as shown in the next section.

https://doi.org/10.5194/egusphere-2026-523
Preprint. Discussion started: 6 February 2026

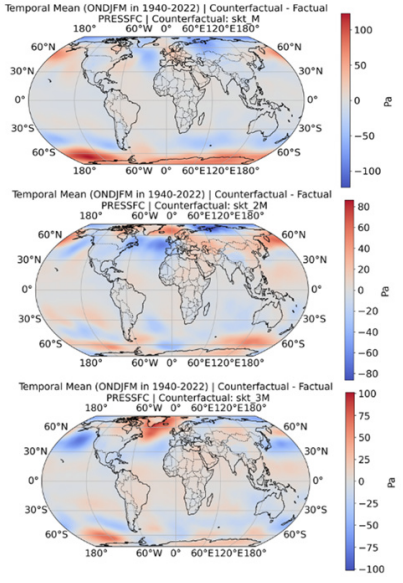

Figure 11. Temporal mean of differences $\bar{\Delta}$ between the counterfactual and factual world for surface pressure. Rows indicate the scenario with increasing amplification of M from top to bottom.

https://doi.org/10.5194/egusphere-2026-523
Preprint. Discussion started: 6 February 2026

8.4.2 Differences in zonal and meridional mean wind speed

We look at the absolute differences in the zonal and meridional wind between the counterfactual and factual world, because the sign of the variables indicates the direction of the winds. For example, if $U_{\text{Counterfactual}} = -15$ m/s and $U_{\text{Factual}} = -10$ m/s then the difference $\Delta = U_{\text{Counterfactual}} - U_{\text{Factual}} = -5$ m/s, but the counterfactual has stronger wind speed in westward direction. We compute the absolute differences similarly to Equation 4 but applying the absolute norm to each side, i.e.

$$|\Delta| = |X_{\text{Counterfactual}}| - |X_{\text{Factual}}|.$$

In order to check whether the actual wind speed of the meridional and zonal winds is different, independent of their direction.

Zonal Wind Speed: The temporal mean of the absolute differences in the zonal wind components is depicted in Fig. 12 for different scenarios.

When looking at UGRD10M (left column), two major signals emerge, one situated in the Southern Circumpolar Current and another in the North Atlantic. The signal in the North Atlantic shows a dipole pattern, with weaker winds near the poles and the equator and stronger winds in the region of the Gulf Stream. Interestingly, the signal in the Southern Hemisphere weakens as the forcing amplification increases, leaving only signals in the North Atlantic and the Pacific. This strengthens the hypothesis that the forcing pattern M is connected to the storm variability in the NH.

For the wind variables at 600 hPa (central column) and 250 hPa (right column), similar differences emerge between the counterfactual and factual. Two major signals are obtained, again at the Southern Circumpolar Current and also in the NH regions of the Jet-Stream. The signal in the SH weakens with increasing amplification and increases in the NH. It seems that the Jet-Stream is shifted in the counterfactual world, indicated by stronger winds poleward and equatorward and weaker winds between 30°N and 50°N. The signals show a wave-like pattern, which could resemble a shift in the Rossby wave patterns.

https://doi.org/10.5194/egusphere-2026-523
Preprint. Discussion started: 6 February 2026

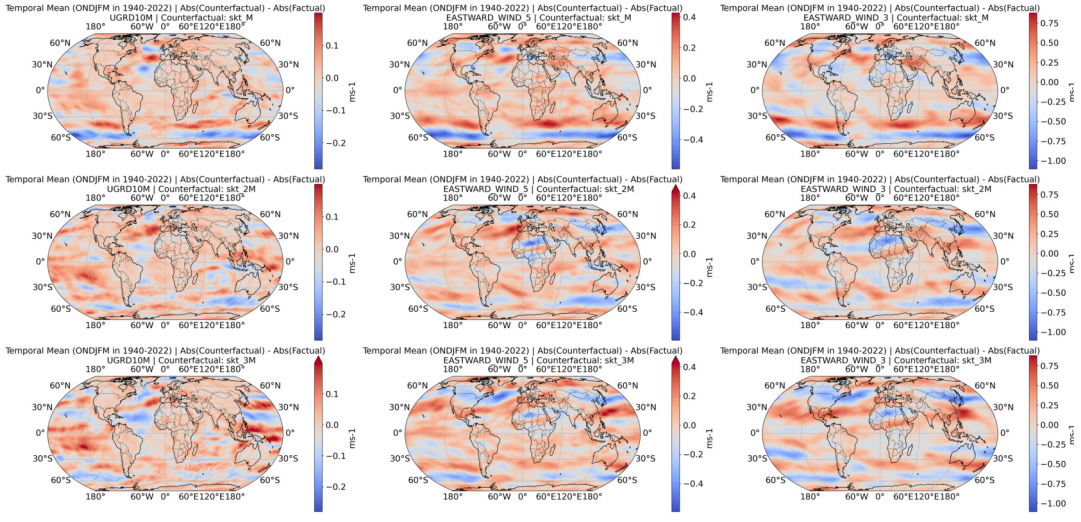

Figure 12. Temporal mean of differences $|\bar{\Delta}|$ between the counterfactual and factual world for zonal wind components. Columns correspond to the wind variables increasing in altitude from left to right. Rows indicate the scenario with increasing amplification of M from top to bottom.

https://doi.org/10.5194/egusphere-2026-523
Preprint. Discussion started: 6 February 2026

Meridional Wind Speed: The temporal mean of $|\Delta|$ of the meridional winds is generally noisier compared to the differences in zonal wind speed (see Fig. 13). The 10m meridional wind speed (left column) is enhanced in the ENSO-Region, i.e the Central Pacific. A mild increase of meridional wind speed can also be seen in the North Atlantic, which is in accordance with the pattern of pressure gradients in that region (see Fig. 11).

A clear signal in the NH can be seen for the meridional winds at around 600 hPa (central column) and 250 hPa (right column), both showing similar differences. Wind speeds are higher over land north of 50°N, e.g., over large parts of Scandinavia, Russia, and Asia. This resembles parts of the spatial variability of the storm index e_1 (see 2). It seems that meridional winds shift eastward in the North Atlantic basin, showing a dipole pattern between 60°W and 50°W.

https://doi.org/10.5194/egusphere-2026-523
Preprint. Discussion started: 6 February 2026

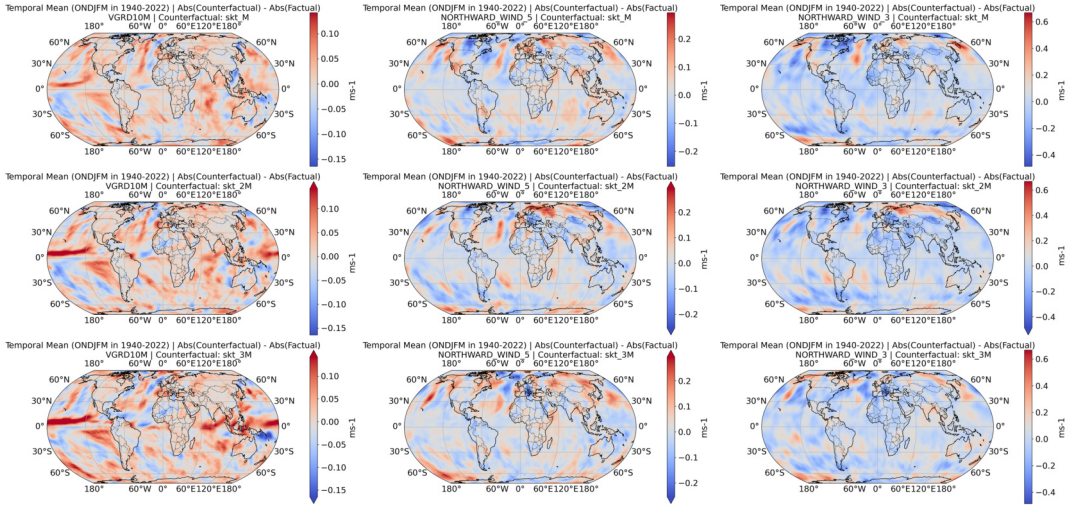

Figure 13. Temporal mean of differences $|\bar{\Delta}|$ between the counterfactual and factual world for meridional wind components. Columns correspond to the wind variables increasing in altitude from left to right. Rows indicate the scenario with increasing amplification of M from top to bottom.

https://doi.org/10.5194/egusphere-2026-523
Preprint. Discussion started: 6 February 2026

8.4.3 Differences in mean wind speed

The differences of wind speed at different altitudes between the counterfactual and factual world are shown in Fig. 14. The top row shows the wind speed of the factual world. Other rows show the difference to the counterfactual world with increasing amplification of the forcing M from top to bottom. Columns show the 10m surface wind speed (left), wind speed at 600 hPa (centre) and wind speed at 250 hPa (right).

The factual world clearly shows strong winds in the Jet Stream Region of the NH and around the Southern Circumpolar Current. These patterns are shifted in the counterfactual world.

10m Surface wind speed (left column): Compared to the factual world, the strong winds in the Southern Ocean shift towards the equator. In the NH the strongest difference in wind speed is obtained in the North Atlantic close to the Gulf Stream region for all scenarios. For an amplified forcing, a signal also emerges in the Central and Western Pacific. In general, the wind speed is slightly increased over land masses of Europe and Asia, suggesting a causal relationship between the surface temperature forcing and higher wind speed at 10m surface level over land regions in the NH.

Wind Speed at 600 hPa (central column) and 250 hPa (right column): Similarly to the surface-level wind speed, the signal is more pronounced in the SH if the forcing is not amplified, and it increases in the NH with increasing M-amplification. There seems to be a split in the Jet-Stream position with higher wind speed towards the equator and the north pole. This split becomes more apparent for an amplified forcing.

https://doi.org/10.5194/egusphere-2026-523
Preprint. Discussion started: 6 February 2026

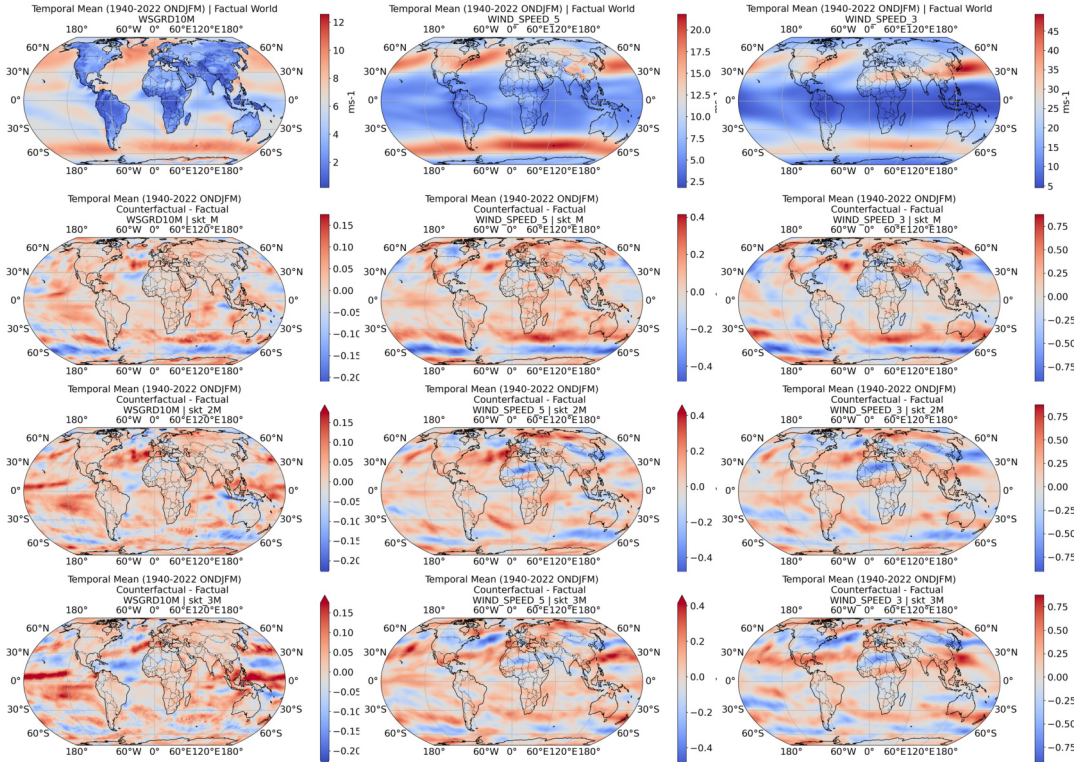

Figure 14. Temporal mean of differences $\bar{\Delta}$ between the counterfactual and factual world for wind speed W. Columns correspond to the wind variables increasing in altitude from left to right. The top row shows the wind speed of the factual world. Rows below the top row show scenarios with increasing amplification from top to bottom.

https://doi.org/10.5194/egusphere-2026-523
Preprint. Discussion started: 6 February 2026

8.4.4 Comparing percentiles of wind speed

Since the storm index developed in this study is based on the 95th-percentile of local wind speed, we compare the change in those percentiles computed over the ONDJFM months in each ensemble. We expect that the counterfactual world has higher percentiles, especially in regions associated with the loading pattern e_1, since the surface-temperature forcing was designed by relating SKT to the temporal structure of e_1.

Figure 15 shows the 95th-percentile of wind speed of the factual world in the top row and the corresponding differences to the counterfactual world for all scenarios and wind speed variables below the top row. The percentiles of the factual world show the typical distribution of wind speeds, with high wind speeds in the region of the Southern Circumpolar Current at all vertical levels, higher wind speeds over the oceans in the NH compared to landmasses at surface level and the pattern of the Jet Stream at altitudes of 600 hPa and 250 hPa.

Changes of the 95th-percentile of wind speed at surface level (left column): Percentiles in the counterfactual worlds are slightly increased over large parts of the NH landmasses. The strongest difference in percentiles can be seen in the North Atlantic close to the Gulf-Stream Region. This difference increases with increasing amplitude of the additional boundary conditions. Even though these boundary conditions were designed to increase the storminess over landmasses in the NH, the strongest difference is seen over the North Atlantic and the Western Pacific. This suggests a connection between the storminess over oceans and subsequently over landmasses.

Changes of the 95th-percentile of wind speed at 600 hPa (central column) and 250 hPa (right column) altitude: For the wind speed at 250 hPa we can again see the split of the Jet Stream in the counterfactual world. The percentiles are higher towards the pole and equator, showing a dipole pattern in the North Atlantic that strengthens with increasing forcing. This pattern is less noisy at the 600 hPa vertical level.

Even though these patterns suggest an increased storminess over land regions that are highlighted by the loadings e_1, the signal is not as clear as expected. To filter the influence of the forcing on the storm variability over land regions more clearly, we build composites of the PC-score a_1.

https://doi.org/10.5194/egusphere-2026-523
Preprint. Discussion started: 6 February 2026

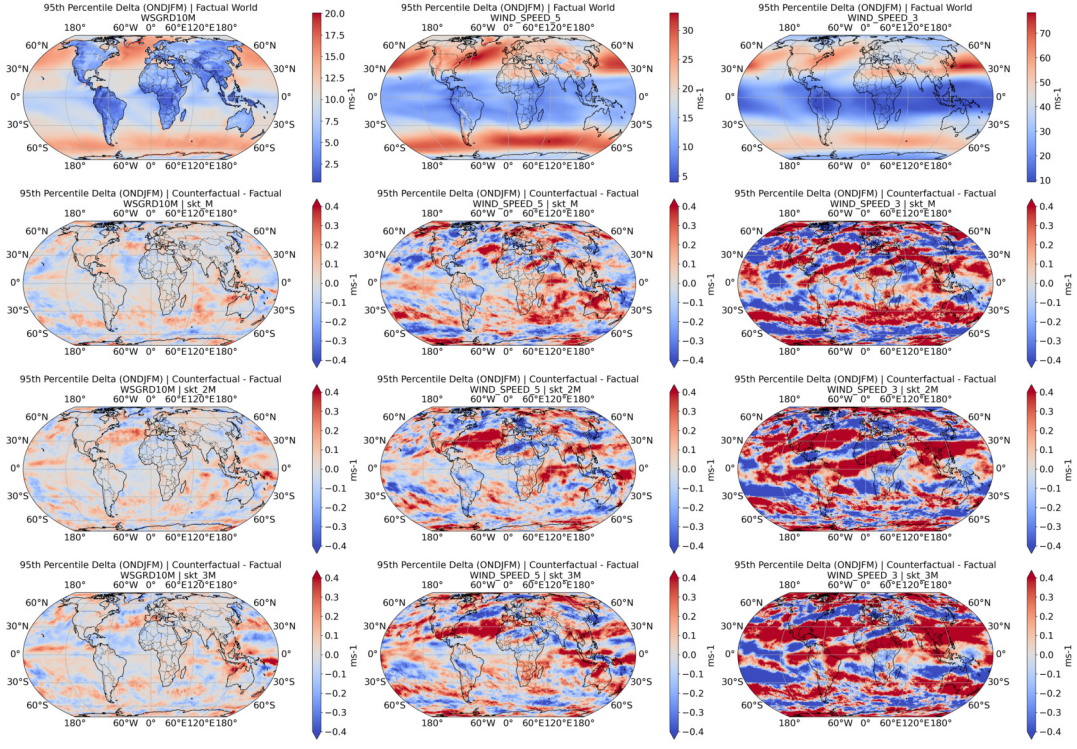

Figure 15. 95th-percentile of wind speed in the factual world (top row) and the differences to the counterfactual world (rows below top row). Columns correspond to the wind variables increasing in altitude from left to right. Rows below the top row show simulation scenarios with increasing amplification of the surface temperature forcing $\tilde{F}$ from top to bottom.

https://doi.org/10.5194/egusphere-2026-523
Preprint. Discussion started: 6 February 2026

8.4.5 Comparing composites of wind speed

We build composites of the 20% highest and lowest values in the timeseries of the PC-Score $a_1(t)$ and call the set of the corresponding dates T_{max} and T_{min}. For each composite, we look at the differences in wind speed between the counterfactual and factual world. We expect to resemble a similar signal as it is obtained in the first mode of spatial storm variability pattern e_1 (see Fig. 2). The red regions of the loading pattern e_1 should be noted as a stronger signal in the analysis of T_{max} composite and the blue regions should show an emphasised signal in the T_{min} composite. It is noted that the signals obtained in the composite might slightly deviate from the loading pattern due to the internal variability of the climate emulator ACE2.

We build the composite by applying the following steps. First, we compute the differences Δ for the daily wind speed data W and average the differences over the ONDJFM season, leaving one spatial map of differences for each storm season (i.e. ensemble member). We select the seasons corresponding to the minimum and maximum composites by sampling from T_{min} and T_{max} and compute the mean over each composite. We repeat this process for each wind speed variable and scenario.

Minimum Composites: Figure 16 shows the wind speed delta for the minimum composite. The minimum composites should show a stronger signal (red in Fig. 16) in the blue regions of the loading pattern e_1 and a lower signal (blue in Fig. 16) in the red regions of e_1. One can indeed see that there is a small correspondence between the signal obtained and e_1, especially for the wind speed at 600 hPa (central column) and 250 hPa (right column) over Europe and Asia.

https://doi.org/10.5194/egusphere-2026-523
Preprint. Discussion started: 6 February 2026

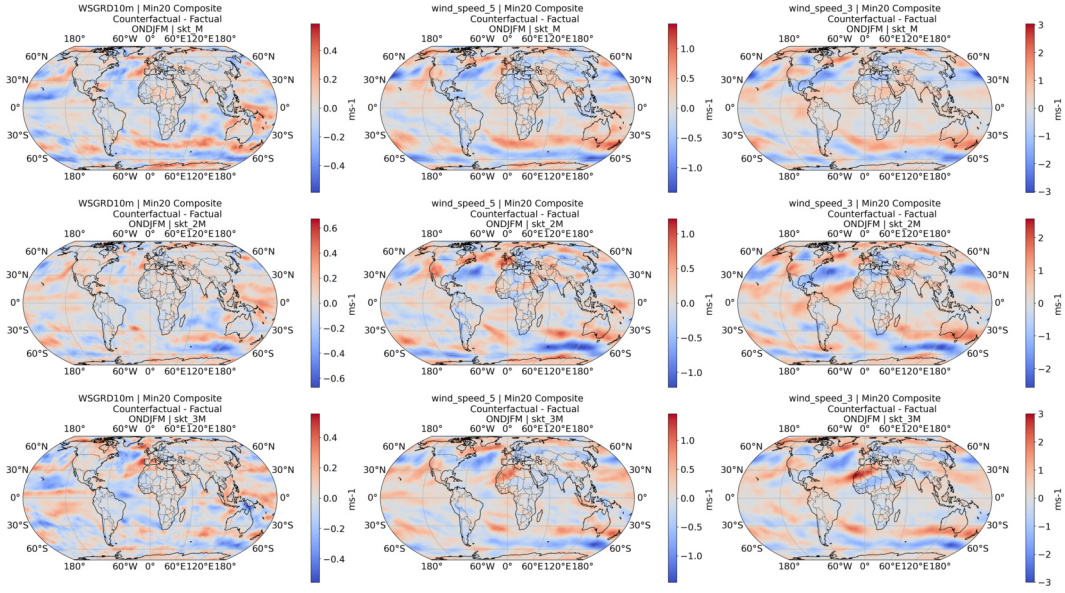

Figure 16. Temporal mean of differences $\bar{\Delta}$ between the counterfactual and factual world for wind speed at different altitudes within the minimum composite sampled from T_{min}. Columns correspond to the wind variables increasing in altitude from left to right. Rows indicate the scenario with increasing amplification of M from top to bottom.

https://doi.org/10.5194/egusphere-2026-523
Preprint. Discussion started: 6 February 2026

Maximum Composites: Figure 17 shows the differences in wind speed between the counterfactual and factual world for the maximum composite. The maximum composites should show a higher signal (red in Fig. 17) in the red regions of the loading pattern e_1 and a lower signal (blue in Fig. 17) in the blue regions of e_1. Indeed the pattern of e_1 is resembled in the maximum composites, especially over Europe and Asia. Wind speeds are generally higher in the red regions of e_1 and lower in the blue regions of e_1.

https://doi.org/10.5194/egusphere-2026-523
Preprint. Discussion started: 6 February 2026

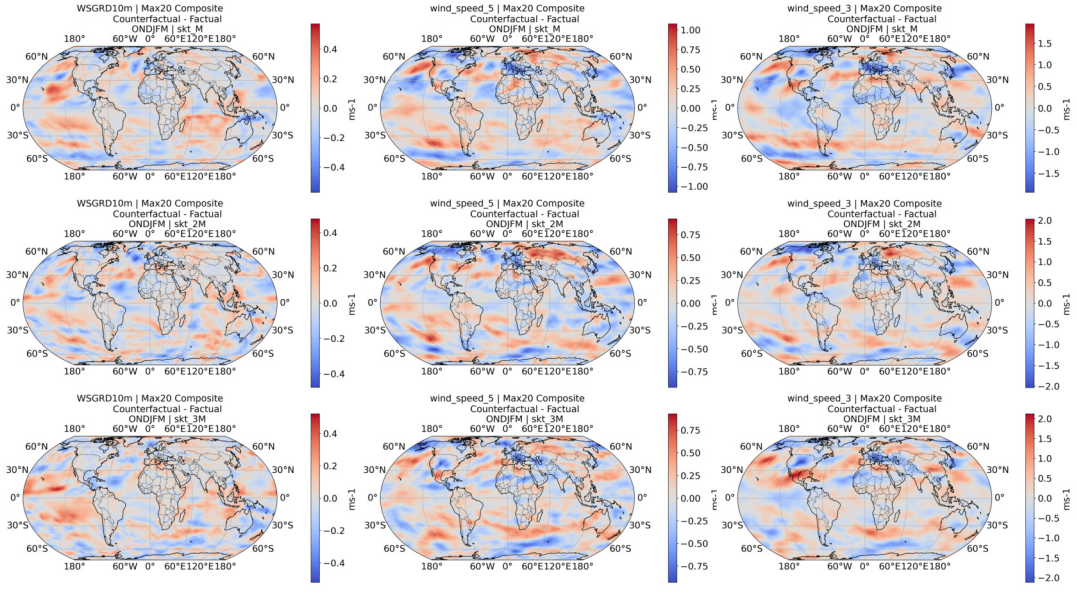

Figure 17. Temporal mean of differences $\bar{\Delta}$ between the counterfactual and factual world for wind speed at different altitudes within the minimum composite sampled from $T_{\max}$. Columns correspond to the wind variables increasing in altitude from left to right. Rows indicate the scenario with increasing amplification of M from top to bottom.

https://doi.org/10.5194/egusphere-2026-523
Preprint. Discussion started: 6 February 2026

In comparison to the pattern in the minimum composite, the correspondence to e_1 is more clearly in the maximum composite. There is also a dipole contrast between the signal obtained in the maximum composite and the one in the minimum composite, which supports the hypothesis that the surface temperature forcing pattern M is causing the storm variability in the loadings e_1. In both composites the loading pattern of the region in the US was not sufficiently recovered. The composite analysis shows that the forcing is successfully exciting the first mode of storm variability over the NH and the emulator responds in a dynamically consistent way. Even if the correlations from the composite analysis do not perfectly match the loadings e_1, it reveals a structured response.

9 Discussion

We identified coherent regions of storm variability over NH landmasses and explored their physical drivers and sensitivity to surface temperature forcing. The first mode of variability of the storm index reveals a pronounced north–south dipole structure over Eurasia, separating regions north and south of approximately 50° N, with synchronous variability within each band and opposite sign between them. This large-scale pattern resembles results of previous studies showing a north-south contrast (Gulev et al., 2001; Zeng et al., 2019; Laurila et al., 2021). Laurila et al. (2021) and (Zeng et al., 2019) both show a dipole in the storm activity between Northern and Southern Europe. Zeng et al. (2019) and (Gulev et al., 2001) explain this contrast by the influence of the NAO, which is supported by the significant correlation between the NAO index and the PC score a_1 obtained in our study. Donat et al. (2011) and Gregow et al. (2020) analysed projected future changes in wind speed percentiles at different pressure levels over Europe and Scandinavia. Their results indicate a north-south contrast in changes of wind speed with a split at the 50°N latitude. Information on this dipole in storm variability is useful for mitigation planning and for managing financial aid funding. For example, financial aid could flow from non-affected to impacted regions, according to this pattern of synchrony in storm variability.

Correlation patterns between SST, MSLP and the storm variability index a_1 suggest a linkage between climate modes and NH storm variability. We found negative SST correlations in the North Atlantic and central–eastern Pacific, which point to the influence of the AMOC and ENSO systems on wind extremes. Both systems are known to modulate baroclinicity and jet-stream strength (McDonald, 2011; Shaw et al., 2016; Delworth et al., 2016), which in turn affects the storm variability. The identified dipole in MSLP anomalies aligns with a positive phase of the NAO, which is known to influence the position and strengthen the speed of the westerlies and jet streams, leading to changes in ETC variability over northern latitudes (Woollings et al., 2010; Lodise et al., 2022). The statistically significant positive correlation between the NAO index and the PC-score a_1 further supports this interpretation.

The sensitivity experiments using the ACE2 emulator demonstrate that prescribed SKT anomalies, derived from correlation patterns with the PC-score a_1, can excite in this emulator the storm variability in loading regions. This provides causal support that large-scale surface temperature gradients, especially gradients between the NH land regions and the north pole, can modulate storminess through their influence on atmospheric circulation. Simulations reveal a NAO like pattern in differences of MSLP between the counterfactual and factual world supporting the link between this climate mode and the storm variability.

https://doi.org/10.5194/egusphere-2026-523
Preprint. Discussion started: 6 February 2026

Changes in the zonal wind speed differ depending on the vertical level, which agrees with the findings of Shaw et al. (2016), who show the importance of the vertical temperature gradient when analyzing storm track responses. The patterns of MSLP differences fit into the changes of zonal and meridional winds suggesting a physical robust reaction of the climate emulator to the forcing.

The emulator experiments reveal increased surface and upper-level wind speeds in the loading regions, particularly over Europe and Asia, along with a poleward–equatorward split of the jet stream. The split of the jet might explain the spatially opposing loadings with the poleward (equatorward) jet core driving storm variability north (south) of the 50°N latitude. This argument is supported by Laurila et al. (2021), which show that a poleward (equatorward) shift of the jet stream increases (weakens) the surface level wind speed in Northern Europe. Woollings et al. (2010) also note that the jet streams deviate from their mean location over the central North Atlantic depending on the NAO state into either a northern or southern jet. This supports our observation of the jet stream split into two branches and the discovered linkage to the NAO, and it seems to drive the meridional contrast in the storm variability.

10 Conclusion

While prior work has described regional storm tracks and their trends, this study provides a new perspective on large-scale synchrony of storminess over NH land regions, combining empirical and dynamical analyses to uncover how wind extremes co-vary and respond to surface thermal forcing. Using a storm index based on local 95th percentile wind speed exceedances for 1940–2023, we identify a leading mode of storm variability that exhibits a clear north–south dipole structure, with synchronous storminess north of 50° N (Europe–Asia) and opposite-phase variability south of 50 ° N. This pattern adds to a previously underexplored dimension of storm behaviour: a hemispheric-scale coordination of wind extremes across distant land areas. Correlation analyses show that this synchronous variability is dynamically linked to large-scale climate modes, such as NAO and ENSO, which modulate baroclinicity and jet-stream strength. These connections demonstrate that regional wind extremes respond to global variability.

By forcing the ACE2 climate emulator with surface temperature anomalies derived from the observed correlations, we show that this forcing can reproduce and enhance the storm variability pattern obtained by the PCA. This strongly suggests a physical causal link between surface temperature gradients and storm synchronisation, and suggests a split in the jet stream to a more poleward and equatorward location as main contributions to the north-south contrast in the storm variability. In addition, we find a meridional temperature gradient between the 40°N - 60°N and the Arctic region and a zonal temperature gradient between the Eurasian and North American continent as possible drivers of the north-south contrast in storm variability over Europe and Asia.

Several caveats apply to this research. By applying PCA, we assume linearity, which is an oversimplified assumption. This is reflected in a modest explained variance of the leading PCA modes, indicating the complexity of the storm variability and implying that higher-order components may contain additional regional information. We only obtain data from one reanalysis product (ERA5) and analyse data prior to the satellite era, which introduces biases and uncertainties in storm representation. We

https://doi.org/10.5194/egusphere-2026-523
Preprint. Discussion started: 6 February 2026

assessed results only from historical simulations from one machine-learning-based climate emulator in the driver-sensitivity analysis, leaving room for model uncertainty.

The use of the ACE2 emulator as a substitute for proper simulations with an Earth System model offers a very clear advantage - namely, the speed and flexibility of conducting atmospheric simulations with different forcings, boundary and initial conditions - but also some points need to be considered. The trained ACE2 emulator essentially has learned the high-frequency autoregressive correlations in a set of 6-hourly means of atmospheric variables (including CO_2 concentrations and solar irradiance). Nevertheless, ACE2 has been shown to reproduce decadal and climate-scale variability (Watt-Meyer et al., 2024), although the mechanisms underlying this capability are not yet fully clear. Here, we have applied ACE2 to explore changes in climate statistics when surface boundary conditions are altered and sustained over longer periods, which, in reality, amounts to testing whether the ACE2 emulator has captured, during training, the temporal alignment between variability in climate statistics and the low-frequency variability in the surface boundary conditions in the ERA5 data set. The interpretation of the changes in the ACE2 output as *causal reaction* to sustained changes in the boundary conditions requires, therefore, the assumption that the temporal alignment of low-frequency statistics is not artificially built-in by the high-frequency training.

Future research could overcome some of the mentioned caveats by (1) incorporating data from different reanalysis products and adding new dynamical predictors such as upper-tropospheric vorticity and eddy kinetic energy, (2) exploring nonlinear relationships between storm variability and boundary forcing using causal networks (similar to Pfleiderer et al. (2020)) or machine learning, and (3) assessing projected changes in the identified storm modes under future warming scenarios using CMIP6 or emulator ensembles. Additionally, one could (4) quantify damage synchrony to improve coordinated risk management by combining our approach with data on wind damages or power outage datasets. In summary, this study advances understanding of how and why wind extremes across the NH vary in concert, linking statistical coherence to physical drivers and providing a new pathway for diagnosing and predicting large-scale storm variability.

.

https://doi.org/10.5194/egusphere-2026-523
Preprint. Discussion started: 6 February 2026

Author contribution

All authors contributed to develop the original research goal, analysed and discussed the results. K.B. coded the software, carried out the data analysis, and drafted the initial versions of the manuscript. B.H and E.Z contributed to the later and final version of the manuscript.

Competing interests

We declare that we have no competing interests.

Acknowledgments

The ERA5 data (Hersbach et al., 2018) were downloaded from the Copernicus Climate Change Service (C3S) Climate Data Store. The results contain modified Copernicus Climate Change Service information 2020. Neither the European Commission nor ECMWF is responsible for any use that may be made of the Copernicus information or data it contains. We thank the authors of the ACE2 emulator (Watt-Meyer et al., 2025) for providing a trained version of their model to the research community. The study was partially funded by the Deutsche Forschungsgemeinschaft (DFG, German Research Foundation) under Germany's Excellence Strategy – EXC 2037 'CLICCS - Climate, Climatic Change, and Society' – Project Number: 390683824.

https://doi.org/10.5194/egusphere-2026-523
Preprint. Discussion started: 6 February 2026

References

Athanasiadis, P. J., Yeager, S., Kwon, Y.-O., Bellucci, A., Smith, D. W., and Tibaldi, S.: Decadal predictability of North Atlantic blocking and the NAO, npj Climate and Atmospheric Science, 3, 20, https://doi.org/10.1038/s41612-020-0120-6, publisher: Nature Publishing Group, 2020.

Behr, H. D.: Trends and Interdependence of Solar Radiation and Air Temperature—A Case Study from Germany, Meteorology, 1, 341–354, https://doi.org/10.3390/meteorology1040022, publisher: Multidisciplinary Digital Publishing Institute, 2022.

Bellomo, K., Angeloni, M., Corti, S., and von Hardenberg, J.: Future climate change shaped by inter-model differences in Atlantic meridional overturning circulation response, Nature Communications, 12, 3659, https://doi.org/10.1038/s41467-021-24015-w, 2021.

Bouwer, L. M., Cheong, S.-M., Jacot Des Combes, H., Frölicher, T. L., McInnes, K. L., Ratter, B. M. W., and Rivera-Arriaga, E.: Risk Management and Adaptation for Extremes and Abrupt Changes in Climate and Oceans: Current Knowledge Gaps, Frontiers in Climate, 3, https://doi.org/10.3389/fclim.2021.785641, publisher: Frontiers, 2022.

Crawford, A. D., McCrystall, M. R., Lukovich, J. V., and Stroeve, J. C.: The Response of Extratropical Cyclone Propagation in the Northern Hemisphere to Global Warming, https://doi.org/10.1175/JCLI-D-23-0082.1, section: Journal of Climate, 2023.

Delworth, T. L., Zeng, F., Vecchi, G. A., Yang, X., Zhang, L., and Zhang, R.: The North Atlantic Oscillation as a driver of rapid climate change in the Northern Hemisphere, Nature Geoscience, 9, 509–512, https://doi.org/10.1038/ngeo2738, publisher: Nature Publishing Group, 2016.

Dogar, M. M., Fujiwara, M., Zhao, M., Ohba, M., and Kosaka, Y.: ENSO and NAO Linkage to Strong Volcanism and Associated Post-Volcanic High-Latitude Winter Warming, Geophysical Research Letters, 51, e2023GL106 114, https://doi.org/10.1029/2023GL106114, _eprint: https://agupubs.onlinelibrary.wiley.com/doi/pdf/10.1029/2023GL106114, 2024.

Donat, M. G., Leckebusch, G. C., Wild, S., and Ulbrich, U.: Future changes in European winter storm losses and extreme wind speeds inferred from GCM and RCM multi-model simulations, Natural Hazards and Earth System Sciences, 11, 1351–1370, https://doi.org/10.5194/nhess-11-1351-2011, publisher: Copernicus GmbH, 2011.

Eichler, T. and Higgins, W.: Climatology and ENSO-Related Variability of North American Extratropical Cyclone Activity, https://doi.org/10.1175/JCLI3725.1, section: Journal of Climate, 2006.

Feser, F.: Constructing Records of Storminess, in: Oxford Research Encyclopedia of Climate Science, https://doi.org/10.1093/acrefore/9780190228620.013.5, 2018.

François, B., Teber, K., Brett, L., Leeding, R., Gimeno-Sotelo, L., Domeisen, D. I. V., Suarez-Gutierrez, L., and Bevacqua, E.: Concurrent modes of climate variability linked to spatially compounding wind and precipitation extremes in the Northern Hemisphere, Earth System Dynamics, 16, 1029–1051, https://doi.org/10.5194/esd-16-1029-2025, publisher: Copernicus GmbH, 2025.

Gray, S. L., Volonté, A., Martínez-Alvarado, O., and Harvey, B. J.: A global climatology of sting-jet extratropical cyclones, EGUsphere, pp. 1–31, https://doi.org/10.5194/egusphere-2024-1413, publisher: Copernicus GmbH, 2024.

Gregow, H., Laurila, T. K., Mäkelä, A., and Rantanen, M.: Review on winds, extratropical cyclones and their impacts in Northern Europe and Finland, Tech. rep., Finnish Meteorological Institute, https://doi.org/10.35614/isbn.9789523361188, 2020.

Gulev, S. K., Zolina, O., and Grigoriev, S.: Extratropical cyclone variability in the Northern Hemisphere winter from the NCEP/NCAR reanalysis data, Climate Dynamics, 17, 795–809, https://doi.org/10.1007/s003820000145, 2001.

Hawcroft, M. K., Shaffrey, L. C., Hodges, K. I., and Dacre, H. F.: How much Northern Hemisphere precipitation is associated with extratropical cyclones?, Geophysical Research Letters, 39, 2012GL053 866, https://doi.org/10.1029/2012GL053866, 2012.

https://doi.org/10.5194/egusphere-2026-523
Preprint. Discussion started: 6 February 2026

Hersbach, H., Bell, B., Berrisford, P., Hirahara, S., Horányi, A., Muñoz-Sabater, J., Nicolas, J., Peubey, C., Radu, R., Schepers, D., Simmons, A., Soci, C., Abdalla, S., Abellan, X., Balsamo, G., Bechtold, P., Biavati, G., Bidlot, J., Bonavita, M., De Chiara, G., Dahlgren, P., Dee, D., Diamantakis, M., Dragani, R., Flemming, J., Forbes, R., Fuentes, M., Geer, A., Haimberger, L., Healy, S., Hogan, R. J., Hólm, E., Janisková, M., Keeley, S., Laloyaux, P., Lopez, P., Lupu, C., Radnoti, G., de Rosnay, P., Rozum, I., Vamborg, F., Villaume, S., and Thépaut, J.-N.: The ERA5 global reanalysis, Quarterly Journal of the Royal Meteorological Society, 146, 1999–2049, https://doi.org/10.1002/qj.3803, _eprint: https://rmets.onlinelibrary.wiley.com/doi/pdf/10.1002/qj.3803, 2020.

Hsieh, W. W.: Introduction to environmental data science, Cambridge University Press, New York, 2023.

Intergovernmental Panel on Climate Change (IPCC): Climate Phenomena and their Relevance for Future Regional Climate Change, p. 1217–1308, Cambridge University Press, https://doi.org/10.1017/CBO9781107415324.028, 2014.

Klotzbach, P., Blake, E., Camp, J., Caron, L.-P., Chan, J. C. L., Kang, N.-Y., Kuleshov, Y., Lee, S.-M., Murakami, H., Saunders, M., Takaya, Y., Vitart, F., and Zhan, R.: Seasonal Tropical Cyclone Forecasting, Tropical Cyclone Research and Review, 8, 134–149, https://doi.org/10.1016/j.tcrr.2019.10.003, 2019.

Laurila, T. K., Sinclair, V. A., and Gregow, H.: Climatology, variability, and trends in near-surface wind speeds over the North Atlantic and Europe during 1979–2018 based on ERA5, International Journal of Climatology, 41, 2253–2278, https://doi.org/10.1002/joc.6957, _eprint: https://onlinelibrary.wiley.com/doi/pdf/10.1002/joc.6957, 2021.

Lim, Y.-K., Cullather, R. I., Nowicki, S. M. J., and Kim, K.-M.: Inter-relationship between subtropical Pacific sea surface temperature, Arctic sea ice concentration, and North Atlantic Oscillation in recent summers, Scientific Reports, 9, 3481, https://doi.org/10.1038/s41598-019-39896-7, publisher: Nature Publishing Group, 2019.

Lodise, J., Merrifield, S., Collins, C., Rogowski, P., Behrens, J., and Terrill, E.: Global Climatology of Extratropical Cyclones From a New Tracking Approach and Associated Wave Heights From Satellite Radar Altimeter, Journal of Geophysical Research: Oceans, 127, e2022JC018 925, https://doi.org/10.1029/2022JC018925, _eprint: https://onlinelibrary.wiley.com/doi/pdf/10.1029/2022JC018925, 2022.

McDonald, R. E.: Understanding the impact of climate change on Northern Hemisphere extra-tropical cyclones, Climate Dynamics, 37, 1399–1425, https://doi.org/10.1007/s00382-010-0916-x, 2011.

Merryfield, W. J., Baehr, J., Batté, L., Becker, E. J., Butler, A. H., Coelho, C. A. S., Danabasoglu, G., Dirmeyer, P. A., Doblas-Reyes, F. J., Domeisen, D. I. V., Ferranti, L., Ilynia, T., Kumar, A., Müller, W. A., Rixen, M., Robertson, A. W., Smith, D. M., Takaya, Y., Tuma, M., Vitart, F., White, C. J., Alvarez, M. S., Ardilouze, C., Attard, H., Baggett, C., Balmaseda, M. A., Beraki, A. F., Bhattacharjee, P. S., Bilbao, R., De Andrade, F. M., DeFlorio, M. J., Díaz, L. B., Ehsan, M. A., Fragkoulidis, G., Grainger, S., Green, B. W., Hell, M. C., Infanti, J. M., Isensee, K., Kataoka, T., Kirtman, B. P., Klingaman, N. P., Lee, J.-Y., Mayer, K., McKay, R., Mecking, J. V., Miller, D. E., Neddermann, N., Justin Ng, C. H., Ossó, A., Pankatz, K., Peatman, S., Pegion, K., Perlwitz, J., Recalde-Coronel, G. C., Reintges, A., Renkl, C., Solaraju-Murali, B., Spring, A., Stan, C., Sun, Y. Q., Tozer, C. R., Vigaud, N., Woolnough, S., and Yeager, S.: Subseasonal to Decadal Prediction: Filling the Weather–Climate Gap, Bulletin of the American Meteorological Society, 101, 767–770, https://doi.org/10.1175/BAMS-D-19-0037.A, 2020.

National Centers for Environmental Information (NCEI): North Atlantic Oscillation (NAO) Index, https://www.ncei.noaa.gov/access/monitoring/nao, accessed: 2025-10-26, 2025.

Pfahl, S. and Wernli, H.: Quantifying the Relevance of Cyclones for Precipitation Extremes, Journal of Climate, 25, 6770–6780, https://doi.org/10.1175/JCLI-D-11-00705.1, 2012.

Pfleiderer, P., Schleussner, C.-F., Geiger, T., and Kretschmer, M.: Robust Predictors for Seasonal Atlantic Hurricane Activity Identified with Causal Effect Networks, https://doi.org/10.5194/wcd-2020-7, 2020.

https://doi.org/10.5194/egusphere-2026-523
Preprint. Discussion started: 6 February 2026

Priestley, M. D. K. and Catto, J. L.: Future changes in the extratropical storm tracks and cyclone intensity, wind speed, and structure, Weather and Climate Dynamics, 3, 337–360, https://doi.org/10.5194/wcd-3-337-2022, publisher: Copernicus GmbH, 2022.

Renggli, D., Leckebusch, G. C., Ulbrich, U., Gleixner, S. N., and Faust, E.: The Skill of Seasonal Ensemble Prediction Systems to Forecast Wintertime Windstorm Frequency over the North Atlantic and Europe, Monthly Weather Review, 139, 3052–3068, https://doi.org/10.1175/2011MWR3518.1, publisher: American Meteorological Society Section: Monthly Weather Review, 2011.

Rousi, E., Rust, H. W., Ulbrich, U., and Anagnostopoulou, C.: Implications of Winter NAO Flavors on Present and Future European Climate, Climate, 8, 13, https://doi.org/10.3390/cli8010013, publisher: Multidisciplinary Digital Publishing Institute, 2020.

Scaife, A. A., Arribas, A., Blockley, E., Brookshaw, A., Clark, R. T., Dunstone, N., Eade, R., Fereday, D., Folland, C. K., Gordon, M., Hermanson, L., Knight, J. R., Lea, D. J., MacLachlan, C., Maidens, A., Martin, M., Peterson, A. K., Smith, D., Vellinga, M., Wallace, E., Waters, J., and Williams, A.: Skillful long-range prediction of European and North American winters, Geophysical Research Letters, 41, 2514–2519, https://doi.org/10.1002/2014GL059637, _eprint: https://agupubs.onlinelibrary.wiley.com/doi/pdf/10.1002/2014GL059637, 2014.

Schultz, D. M., Bosart, L. F., Colle, B. A., Davies, H. C., Dearden, C., Keyser, D., Martius, O., Roebber, P. J., Steenburgh, W. J., Volkert, H., and Winters, A. C.: Extratropical Cyclones: A Century of Research on Meteorology's Centerpiece, https://doi.org/10.1175/AMSMONOGRAPHS-D-18-0015.1, section: Meteorological Monographs, 2019.

Seager, R., Liu, H., Kushnir, Y., Osborn, T. J., Simpson, I. R., Kelley, C. R., and Nakamura, J.: Mechanisms of Winter Precipitation Variability in the European–Mediterranean Region Associated with the North Atlantic Oscillation, Journal of Climate, 33, 7179–7196, https://doi.org/10.1175/JCLI-D-20-0011.1, publisher: American Meteorological Society Section: Journal of Climate, 2020.

Shaw, T. A., Baldwin, M., Barnes, E. A., Caballero, R., Garfinkel, C. I., Hwang, Y.-T., Li, C., O'Gorman, P. A., Rivière, G., Simpson, I. R., and Voigt, A.: Storm track processes and the opposing influences of climate change, Nature Geoscience, 9, 656–664, https://doi.org/10.1038/ngeo2783, publisher: Nature Publishing Group, 2016.

Sillmann, J., Kharin, V. V., Zwiers, F. W., Zhang, X., and Bronaugh, D.: Climate extremes indices in the CMIP5 multimodel ensemble: Part 2. Future climate projections, Journal of Geophysical Research: Atmospheres, 118, 2473–2493, https://doi.org/10.1002/jgrd.50188, _eprint: https://onlinelibrary.wiley.com/doi/pdf/10.1002/jgrd.50188, 2013.

Sinclair, V. A., Rantanen, M., Haapanala, P., Räisänen, J., and Järvinen, H.: The characteristics and structure of extra-tropical cyclones in a warmer climate, Weather and Climate Dynamics, 1, 1–25, https://doi.org/10.5194/wcd-1-1-2020, publisher: Copernicus GmbH, 2020.

Ulbrich, U., Leckebusch, G. C., and Pinto, J. G.: Extra-tropical cyclones in the present and future climate: a review, Theoretical and Applied Climatology, 96, 117–131, https://doi.org/10.1007/s00704-008-0083-8, 2009.

von Storch, H., Fennel, K., Jensen, J., Lewis, K. A., Ratter, B., Schlurmann, T., Wahl, T., and Zhang, W.: Climate and Coast: Overview and Introduction, in: Oxford Research Encyclopedia of Climate Science, Oxford University Press, https://doi.org/10.1093/acrefore/9780190228620.013.816, 2021.

von Storch, H., Feser, F., Blender, R., Camargo, S. J., Cavicchia, L., Di Luca, A., Fu, G., Gozzo, L. F., Koks, E., Messmer, M., Mori, N., Priestley, M. D., Roy, T., Schultz, D. M., Watanabe, S.-i., and Weisse, R.: Storms as Forming and Threatening Factors for Coasts, in: Oxford Research Encyclopedia of Climate Science, Oxford University Press, https://doi.org/10.1093/acrefore/9780190228620.013.853, bibtex: vonstorch2024, 2024.

Wang, W., Anderson, B. T., Kaufmann, R. K., and Myneni, R. B.: The Relation between the North Atlantic Oscillation and SSTs in the North Atlantic Basin, Journal of Climate, 17, 4752–4759, https://doi.org/10.1175/JCLI-3186.1, publisher: American Meteorological Society Section: Journal of Climate, 2004.

https://doi.org/10.5194/egusphere-2026-523
Preprint. Discussion started: 6 February 2026

Wang, X. L., Swail, V. R., and Zwiers, F. W.: Climatology and Changes of Extratropical Cyclone Activity: Comparison of ERA-40 with NCEP–NCAR Reanalysis for 1958–2001, Journal of Climate, 19, 3145–3166, https://doi.org/10.1175/JCLI3781.1, 2006.

Watt-Meyer, O., Dresdner, G., McGibbon, J., Clark, S. K., Henn, B., Duncan, J., Brenowitz, N. D., Kashinath, K., Pritchard, M. S., Bonev, B., Peters, M. E., and Bretherton, C. S.: ACE: A fast, skillful learned global atmospheric model for climate prediction, https://doi.org/10.48550/arXiv.2310.02074, arXiv:2310.02074 [physics], 2023.

Watt-Meyer, O., Henn, B., McGibbon, J., Clark, S. K., Kwa, A., Perkins, W. A., Wu, E., Harris, L., and Bretherton, C. S.: ACE2: Accurately learning subseasonal to decadal atmospheric variability and forced responses, https://doi.org/10.48550/arXiv.2411.11268, arXiv:2411.11268 [physics], 2024.

Watt-Meyer, O., Henn, B., McGibbon, J., Clark, S. K., Kwa, A., Perkins, W. A., Wu, E., Harris, L., and Bretherton, C. S.: ACE2: accurately learning subseasonal to decadal atmospheric variability and forced responses, npj Climate and Atmospheric Science, 8, 205, 2025.

Woollings, T., Hannachi, A., and Hoskins, B.: Variability of the North Atlantic eddy-driven jet stream, Quarterly Journal of the Royal Meteorological Society, 136, 856–868, https://doi.org/10.1002/qj.625, _eprint: https://rmets.onlinelibrary.wiley.com/doi/pdf/10.1002/qj.625, 2010.

World Meteorological Organization: Tropical cyclone - World Meteorological Organization, https://wmo.int/topics/tropical-cyclone, accessed: 2025-10-28, 2025.

Wu, R., Sun, H., and Wang, Z.: Individual and combined roles of ENSO and NAO in the development of the North Atlantic tripole SST anomalies during boreal spring, Theoretical and Applied Climatology, 155, 2119–2134, https://doi.org/10.1007/s00704-023-04762-0, 2024.

Zeng, Z., Ziegler, A. D., Searchinger, T., Yang, L., Chen, A., Ju, K., Piao, S., Li, L. Z. X., Ciais, P., Chen, D., Liu, J., Azorin-Molina, C., Chappell, A., Medvigy, D., and Wood, E. F.: A reversal in global terrestrial stilling and its implications for wind energy production, Nature Climate Change, 9, 979–985, https://doi.org/10.1038/s41558-019-0622-6, 2019.

Zhang, X., Alexander, L., Hegerl, G. C., Jones, P., Tank, A. K., Peterson, T. C., Trewin, B., and Zwiers, F. W.: Indices for monitoring changes in extremes based on daily temperature and precipitation data, WIREs Climate Change, 2, 851–870, https://doi.org/10.1002/wcc.147, _eprint: https://onlinelibrary.wiley.com/doi/pdf/10.1002/wcc.147, 2011.